Non-Canonical Targets of HIF1a Drive Cell-Type-Specific Dysfunction

Kevin C. Allan[1], Lucille R. Hu[1], Andrew R. Morton[1], Marissa A. Scavuzzo[1], Artur S. Gevorgyan[1], Benjamin L.L. Clayton[1], Ilya R. Bederman[1], Stevephen Hung[1] Cynthia F. Bartels[1], Mayur Madhavan[1], Paul J. Tesar[1*]

[1]Department of Genetics and Genome Sciences, Case Western Reserve University School of Medicine, Cleveland, Ohio 44106, USA.

***Correspondence:** paul.tesar@case.edu

SUMMARY

All mammalian cells sense and respond to insufficient oxygen, or hypoxia, through the activity of hypoxia-inducible factors (HIFs), an evolutionarily conserved family of transcriptional regulators that promote oxygen-independent energy metabolism and angiogenesis. While HIF activation is transiently protective for all cells, prolonged HIF activity drives distinct pathological responses in different tissues. How HIF achieves this pleiotropic effect is largely unknown. Here, we demonstrate that non-canonical targets of HIF1a impair the function of oligodendrocyte progenitor cells (OPCs) to generate oligodendrocytes. Beyond the canonical gene targets shared between all cell types, HIF1a also bound to and activated a unique set of targets in OPCs including *Ascl2* and *Dlx3*. Each of these targets, when ectopically expressed, was sufficient to block oligodendrocyte development through suppression of the key oligodendrocyte regulator *Sox10*. Chemical screening revealed that inhibition of MEK/ERK signaling overcame the HIF1a-mediated block in oligodendrocyte generation by restoring *Sox10* expression without impacting canonical HIF1a activity. Collectively this work defines the mechanism by which chronic HIF1a suppresses oligodendrocyte formation. More broadly, we establish that cell-type-specific HIF1a targets, independent of the canonical hypoxia response, perturb cell function and drive disease in chronic hypoxia.

INTRODUCTION

The ability to sense and respond to fluctuations in oxygen levels is required to maintain homeostasis in every cell in the body (Kaelin and Ratcliffe, 2008; Semenza, 2012). Insufficient concentrations of molecular oxygen rapidly trigger an evolutionary conserved transcriptional response that enables cell survival in low oxygen by promoting anaerobic metabolism for energy production as well as angiogenesis and erythropoiesis to increase access to local oxygen. While this is initially protective, prolonged activation of this response leads to cellular dysfunction and disease in many tissues. For example, the response to chronic hypoxia blocks white matter formation in premature birth (Scafidi et al., 2014; Volpe, 2009; Volpe et al., 2011), promotes inflammation and insulin resistance in obesity (Lee et al., 2014), and impairs hematopoietic stem cell transplantation capacity (Takubo et al., 2010). This cellular dysfunction has largely been attributed to prolonged activation of the canonical response to low oxygen shared across all cell types; however, it is difficult to explain how activation of a conserved set of hypoxia signature genes can lead to such diverse cellular phenotypes. An alternative unexplored possibility is that cell-type-specific differences in chromatin landscape enable access to unique non-canonical targets, which could account for tissue-specific pathologies.

The response to low oxygen is mediated by hypoxia inducible factors (HIFs), a family of transcription factors that are stabilized under hypoxic conditions in all mammalian cells and are primarily thought to upregulate multiple pathways that adapt cells to low oxygen (Cassavaugh and Lounsbury, 2011; Choudhry and Harris, 2018; Kupferschmidt, 2019). HIFs are heterodimeric complexes consisting of an alpha and beta subunit. In the presence of oxygen, alpha subunits are hydroxylated by prolyl-hydroxylases, allowing for recognition and ubiquitination by von Hippel Lindau (VHL) (Ivan et al., 2001; Jaakkola et al., 2001), and rapid degradation by the proteasome. However, in low oxygen conditions the alpha subunits escape hydroxylation, avoid degradation, and translocate to the nucleus to pair with constitutive beta subunits and regulate gene expression (Cassavaugh and Lounsbury, 2011; Choudhry and Harris, 2018; Semenza, 2007). The HIF1a

59 motif is present more than 1 million times in the genome; however, HIF1a binds to only a small
60 fraction of these sites, which suggests that HIF1a binding is heavily regulated (Schodel et al.,
61 2011; Smythies et al., 2019). Still, the determinants of HIF1a binding in each cell type and whether
62 cell-type-specific targets are functional remain unknown.

63 The central nervous system (CNS) consumes 20% of the body's oxygen supply and white
64 matter of the CNS is highly susceptible to hypoxic insults as seen in stroke, vascular dementia,
65 respiratory distress syndromes, premature birth, and subsets of cerebral palsy (Hankey, 2017;
66 Salmaso et al., 2014; Shindo et al., 2016; Volpe, 2009). In fact, chronic HIF1a activity is sufficient
67 to block white matter development (Yuen et al., 2014). White matter of the CNS is formed by
68 oligodendrocytes, which wrap neuronal axons in a lipid-rich protective sheath called myelin,
69 allowing for rapid transmission of action potentials and maintenance of axonal integrity (Chang et
70 al., 2016; Emery, 2010; Nave, 2010). Oligodendrocytes arise from oligodendrocyte progenitor
71 cells (OPCs), which are prevalent in the developing and adult CNS, and HIF1a accumulation has
72 been shown to be sufficient to impair oligodendrocyte formation from OPCs (Jablonska et al.,
73 2016; van Tilborg et al., 2018; Yuen et al., 2014). However, the mechanism of the HIF1a-mediated
74 block in oligodendrocyte formation from OPCs remains unclear. In this study, we use OPCs as
75 an archetypal hypoxia-disease relevant cell type to define the mechanism by which chronic HIF1a
76 drives cell dysfunction.

77

78 **RESULTS**

79 **Knockout of VHL models chronic HIF1a accumulation in iPSC-derived OPCs**

80 Defining the mechanisms by which HIF activity perturbs cell function is notoriously challenging as
81 HIFs are rapidly degraded, in minutes, when cells are restored to normoxia. Because of this
82 instability and the low abundance of HIFs, biochemical studies often require extraordinary
83 numbers of cells, which is challenging for hypoxia disease relevant cell types outside of cancer
84 cell lines. To explore the mechanisms underlying the HIF-mediated block in oligodendrocyte

85 development from OPCs, we generated a cellular model of chronic HIF1a accumulation in mouse
86 pluripotent stem cell-derived OPCs, which are uniquely scalable and amenable to genetic
87 manipulation (Hubler et al., 2018; Lager et al., 2018; Najm et al., 2015; Najm et al., 2011).
88 CRISPR-Cas9-mediated knockout of VHL, a central component of the ubiquitin-proteasome
89 system that degrades HIFs (Choudhry and Harris, 2018; Haase, 2009; Rechsteiner et al., 2011),
90 in OPC cultures resulted in stable HIF1a protein accumulation and significant 9-fold and 18-fold
91 activation of downstream hallmark HIF1a targets *Vegfa* and *Bnip3*, respectively (Figures 1A, 1B,
92 S1A and S1B). The response of OPCs to VHL knockout mirrored that of OPCs cultured in hypoxia
93 (1% O_2), which led to a significant 11-fold increase in *Vegfa* and 26-fold increase in *Bnip3* (Figures
94 1C and 1D). VHL knockout OPCs were generated with two independent single guide RNAs
95 targeting *Vhl* (sgVhl and sgVhl.2), each of which caused significant decreases in Vhl transcript
96 and protein levels through Cas9-mediated insertion-deletions (in-dels) at the respective target
97 sites compared to control (Cas9 expressing OPCs with no sgRNA) (Figures S1C-S1E). sgVhl
98 OPCs were used for a majority of the data in the study; however, we confirmed key findings in
99 sgVhl.2 OPCs, OPCs treated with physiological hypoxia, primary mouse OPCs exposed to
100 hypoxia, and human OPCs in pluripotent stem cell-derived oligocortical spheroids (Madhavan et
101 al., 2018).
102

103 **HIF1a accumulation specifically delays OPC differentiation into oligodendrocytes**

104 HIF1a accumulation in OPCs is sufficient to impair oligodendrocyte formation (Yuen et al., 2014).
105 To test whether HIF1a accumulation is a general or specific inhibitor of OPC differentiation, sgVhl
106 OPCs were stimulated to form either astrocytes (Grinspan et al., 2000), or oligodendrocytes (Baas
107 et al., 1997; Barres et al., 1994; Gao et al., 1998; Najm et al., 2011) (Figure 1E). This revealed a
108 significant 4-fold reduction in oligodendrocyte formation by staining for myelin basic protein
109 (MBP), a marker of mature oligodendrocytes, with no change in astrocyte formation by staining
110 for glial fibrillary acidic protein (GFAP) in sgVhl OPCs compared to control (Figures 1E-1G, and

111 S1F). This suggests HIF1a specifically blocks oligodendrocyte formation from OPCs; however, at
112 what stage HIF1a accumulation impairs the formation of oligodendrocytes is unknown. Staining
113 for early (O4+), intermediate (O1+), and late (MBP+) oligodendrocyte markers throughout the
114 differentiation process demonstrated a significant and delayed acquisition of all oligodendrocyte
115 markers in sgVhl and sgVhl.2 OPCs compared to control (Figures 1H-1L, and S1G-S1I). These
116 data suggest that HIF1a accumulation impairs early OPC differentiation, thereby delaying the
117 formation of oligodendrocytes and ultimately myelin.
118

119 **HIF1a binds proximal to promoters and indirectly suppresses *Sox10* expression in OPCs**

120 To delineate the gene targets of HIF1a in OPCs responsible for blocking oligodendrocyte
121 development, chromatin-linked immunoprecipitation sequencing (ChIP-seq) was used to map its
122 genome-wide chromatin binding profile. Utilizing 100 million control and sgVhl OPCs for HIF1a
123 ChIP-seq identified 503 high-stringent peaks (FDR<0.001) in sgVhl OPCs with clear enrichment
124 proximal to the annotated transcription start site (TSS), which agrees with HIF1a as a promoter
125 centric transcription factor (Schodel et al., 2011; Smythies et al., 2019) (Figures 2A and S2A).
126 HIF1a was enriched at canonical target genes *Vegfa* and *Bnip3* and globally peaks were enriched
127 for HIF motifs and motifs of transcription factors that have been shown to interact with HIF1a
128 including Sp1, c-Myc, and Bmal1 (Huang, 2008; Kaluz et al., 2003; Wu et al., 2017) (Figures S2A
129 and S2B). HIF1a was not found proximal to *Sirt1*, *Wnt7a*, or *Wnt7b* (Figures S2C-S2E), which
130 have previously been suggested as putative HIF effectors in OPCs (Jablonska et al., 2016; Yuen
131 et al., 2014). Moreover, neither sgVhl OPCs nor wild type OPCs exposed to hypoxia exhibited
132 increased expression of *Sirt1*, *Wnt7a*, or *Wnt7b* transcripts, suggesting that other targets are likely
133 functioning to block oligodendrocyte formation (Figures S2F-S2I) (Zhang et al., 2020).

134 To determine the functional targets of HIF1a, we performed RNA-seq of sgVhl and control
135 OPCs. Overlapping transcripts that significantly changed between sgVhl and control OPCs (P-
136 adj<0.05) with direct targets of HIF1a revealed that HIF1a directly bound to 61 significantly

137 increased genes and only 1 significantly decreased gene (Figure 2B), consistent with the role of
138 HIF1a as a transcriptional activator (Dengler et al., 2014; Guimaraes-Camboa et al., 2015). ChIP-
139 seq for a marker of active chromatin, H3K27Ac (Creyghton et al., 2010), in sgVhl and control
140 OPCs mirrored these findings with a greater number of regions exhibiting a significant gain of
141 H3K27Ac in sgVhl OPCs compared to control (FDR<0.1), and these regions were enriched for
142 HIF motifs (Figures S2J and S2K). To define the top functional targets of HIF1a in OPCs, we
143 overlapped direct HIF1a targets (FDR<0.001) with genes that exhibited both increased
144 transcription (P-adj<0.05) and increased H3K27Ac (FDR<0.1) in sgVhl OPCs compared to control
145 (Figure 2C). Hits were independently validated in OPCs treated with hypoxia, which showed that
146 all of our top 10 HIF1a targets were significantly upregulated compared to normoxia (Figures 1D
147 and 2D).

148 Of note, HIF1a did not bind proximal to any master regulators of oligodendrocyte
149 development, such as Sox10, Olig2, and Nkx2.2. However, the proximal promoter region of
150 *Sox10*, a basic helix loop helix (bHLH) transcription factor required for formation of
151 oligodendrocytes from OPCs (Stolt et al., 2004; Stolt et al., 2002), showed a reduction of H3K27Ac
152 in sgVhl OPCs (Figure 2E). The decrease in H3K27Ac correlated with a reduction of Sox10 mRNA
153 and protein as well as reduction in expression of downstream Sox10 target genes, *Plp1* and
154 *Pdgfra*, in sgVhl OPCs and primary OPCs treated with hypoxia (1% O_2) (Figures 2F, 2G, and S2L-
155 S2N). These data suggest that HIF1a activates gene targets that may ultimately impair expression
156 of *Sox10* to block oligodendrocyte development.

157

158 **Chromatin accessibility and cell-type-specific transcription factors define non-canonical**
159 **HIF1a targets**

160 Whether sustained activation of unique cell-type-specific HIF1a target genes drive cellular
161 dysfunction in hypoxia is unknown. To categorize canonical and cell-type-specific targets of
162 HIF1a, we overlapped HIF1a targets in OPCs with HIF1a targets from the limited number of

163 publicly available datasets derived from other mouse cell types including melanocytes (Loftus et
164 al., 2017), T-cells (Ciofani et al., 2012), and embryonic heart (Guimaraes-Camboa et al., 2015).
165 This analysis identified 51 genes that were HIF1a targets across all 4 cell types ("HIF1a core
166 targets"), 152 genes that were HIF1a targets only in OPCs based on these datasets ("OPC-
167 specific HIF1a targets") and 2250 genes that were specific to either heart, T-cells, or melanocytes
168 ("Other tissue-specific HIF1a targets") (Figure 3A). Both core and OPC-specific HIF1a target
169 genes collectively increased in expression in sgVhl OPCs compared to control, and both of these
170 gene sets showed a significantly greater increase in expression compared to the other tissue
171 specific HIF1a targets in sgVhl OPCs (Figures 3B and S3A).

172 Gene ontology (GO) analysis of core HIF1a target genes showed enrichment for metabolic
173 and hypoxia pathways, which agrees with HIF1a's canonical role to promote glycolysis in a
174 majority of cell types (Figure 3C) (Choudhry and Harris, 2018; Majmundar et al., 2010; Miska et
175 al., 2019; Nagao et al., 2019). In fact, more than half of the enzymes in the glycolysis pathway
176 were direct HIF1a targets in OPCs, and both sgVhl and sgVhl.2 OPCs exhibited a 2-fold increase
177 in levels of the glycolysis byproduct, lactate, compared to control OPCs (Figures 3D and 3E).
178 Interestingly, GO analysis for cell-type-specific HIF1a targets demonstrated enrichment for
179 pathways separate from the canonical hypoxic response and related to the tissue of origin (Figure
180 S3B). In particular, GO analysis for OPC-specific HIF1a targets showed enrichment for neural
181 development and differentiation pathways (Figure 3C).

182 To better understand the determinants of the cell type specificity of HIF1a binding profiles,
183 we compared the chromatin landscape in OPCs at core, OPC-specific, and other tissue-specific
184 HIF1a peaks (Figure S3C). The core and OPC-specific HIF1a peaks exhibited a greater
185 enrichment for HIF1a, H3K27Ac and open chromatin (defined by ATAC-seq regions in non-
186 transduced OPCs) compared to other tissue-specific HIF1a sites (Figure 3F). This agrees with
187 previous findings that HIF1a preferentially binds open and active chromatin (Smythies et al., 2019;
188 Xia and Kung, 2009). However, there was a subset of other tissue specific HIF1a peaks enriched

189 for open and active chromatin that lacked HIF1a binding in OPCs, suggesting that chromatin
190 accessibility and activity were not the sole predictors of HIF1a binding. Motif enrichment analysis
191 under cell-type-specific HIF1a peaks demonstrated an enrichment for lineage defining
192 transcription factors such as the Mitf family in melanocytes (Levy et al., 2006), Nkx2 family in
193 embryonic heart (Bartlett et al., 2010), and basic-helix-loop helix (bHLH) motifs in OPCs (Figure
194 S3D). Specifically, the motif for Olig2, a lineage-defining bHLH transcription factor in OPCs (Yu
195 et al., 2013), was highly enriched (in the top 5% of motifs) under OPC-specific HIF1a peaks,
196 whereas the Olig2 motif was not enriched under any other tissue-specific HIF1a peaks (Figure
197 S3D). Collectively, these data suggest that, outside of canonical HIF1a targets, chromatin
198 accessibility and interaction with lineage defining transcription factors determine HIF1a's unique
199 non-canonical targets in each cell type.
200

201 **Cell-type-specific targets of HIF1a suppress oligodendrocyte formation and *Sox10***
202 **expression**

203 Out of the top 10 targets of HIF1a in OPCs, *Ascl2* and *Dlx3* were the only OPC-specific HIF1a
204 targets (Figure 2C). Both are transcription factors that regulate differentiation of somatic stem
205 cells in the periphery and are not normally expressed by any cell type in the mouse CNS (Tabula
206 Muris et al., 2018; Zhang et al., 2014); however, both accumulate at the protein level in sgVhl
207 OPCs compared to control (Figures S3E-S3G). This is reflected by the lack of active chromatin
208 at *Ascl2* and *Dlx3* loci in control OPCs; however, both demonstrate robust HIF1a peaks proximal
209 to their promoters specifically in sgVhl OPCs compared to heart, melanocytes and T-cells along
210 with gained H3K27Ac in sgVhl OPCs compared to control OPCs (Figure 3G). Activation of both
211 *Ascl2* and *Dlx3* transcripts also validated in primary OPCs treated with hypoxia (1% O_2) compared
212 to normoxia (Figure S3H). In fact, ASCL2 was induced *in vivo* in the brains of mouse pups reared
213 in chronic hypoxia (10% O_2) and this correlated with a decrease in white matter proteins MBP and
214 MAG compared to normoxia reared controls (Figures S3I and S3J).

215 Ectopic expression of Dlx3 and Ascl2 in OPCs using CRISPR activation (CRISPRA)
216 technology was sufficient to impair the acquisition of early (O4+), intermediate (O1+), and late
217 (MBP+) oligodendrocyte markers across the course of differentiation (Figure 3H). Moreover,
218 ectopic expression of Dlx3 and Ascl2 also led to a significant reduction in *Sox10* expression
219 (Figures 3I and S3K), whereas activation of shared HIF1a core targets, *Slc16a3* and *Vegfa*, did
220 not (Figures S3K and S3L). These data demonstrate that non-canonical HIF1a targets are
221 sufficient to impair oligodendrocyte formation and emphasize that cell-type-specific targets of
222 HIF1a play a role in driving cellular dysfunction.
223
224 **Chemical inhibition of MEK/ERK increases oligodendrocyte formation from sgVhl OPCs**
225 To identify potential pathways that could overcome the HIF1a-indcued cellular pathology of OPCs,
226 we tested a library of 1753 bioactive compounds for the ability to increase the formation of MBP+
227 oligodendrocytes relative to DMSO treated sgVhl OPCs, which exhibited a consistent
228 differentiation deficit compared to DMSO treated control OPCs (Figures 4A and S4A-S4D).
229 Compounds that were non-toxic (fold change in total cell number > 0.7 relative to DMSO treated
230 sgVhl OPCs) and enhanced the number and percentage of MBP+ oligodendrocytes (fold change
231 > 3 relative to DMSO treated sgVhl OPCs) were considered primary hits (Figure S4E). MEK
232 inhibitors were enriched among the primary hits and, as a class, demonstrated a significant
233 increase in oligodendrocyte formation compared to all other non-toxic compounds tested in the
234 primary screen (Figures 4B, 4C, and S4F). Interestingly, drugs previously identified to enhance
235 oligodendrocyte formation, such as miconazole and clemastine (Mei et al., 2014; Najm et al.,
236 2015), were not enriched as hits in this screen, highlighting the ability of this screen to identify
237 context-specific modulators of the differentiation block imposed by HIF1a.
238 To identify compounds that were effective across a range of doses, we performed an 8-
239 point dose curve from 10μM to 78nM of the top 14 hits. Performing unbiased hierarchical
240 clustering of the results revealed that all 5 MEK inhibitors clustered together and led to a

241 pronounced increase in oligodendrocyte formation relative to DMSO treated sgVhl OPCs, with
242 AZD8330 and PD0325091 outperforming PD318088 and Selumetinib (Figures 4D, 4E, and S4G).
243 The ability of these different MEK inhibitors to increase oligodendrocyte formation correlated with
244 their on-target IC50 values for MEK1 and MEK2 as well as their on-target ability to reduce ERK1/2
245 phosphorylation in sgVhl OPCs (Figures 4F, 4G, and S4H). Performance of an 8-point dose curve
246 consisting of 12 drugs that each inhibit a potential downstream target of MEK revealed that
247 ERK1/2 inhibitors led to the greatest increase in oligodendrocyte formation compared to the other
248 classes of drugs tested (Shaul and Seger, 2007; Yohe et al., 2018) (Figures S4I and S4J).
249 Collectively, these results demonstrate that chemical inhibition of MEK/ERK acts as a node of
250 intervention to increase the formation of oligodendrocytes in the context of HIF1a accumulation.
251

252 **MEK/ERK inhibition drives *Sox10* expression without changing HIF1a activity**

253 We next asked whether these drugs increased differentiation of sgVhl OPCs by inhibiting HIF1a
254 signaling or circumventing HIF1a by driving genes critical for oligodendrocyte development.
255 Treating OPCs with 300nM AZD8330, our most potent MEK inhibitor (Figures 4F and 4G), for 14
256 hours led to no change in HIF1a translocation to the nucleus compared to DMSO treated sgVhl
257 OPCs (Figure 5A). Performing RNA-seq on control and sgVhl OPCs treated with either DMSO or
258 300nM AZD8330 for 14 hours mirrored these results and demonstrated that AZD8330 treatment
259 did not change HIF1a target gene expression, such as *Ascl2* and *Dlx3*, in sgVhl OPCs compared
260 to DMSO (Figures 5B, 5C, and S5A). This demonstrates that MEK inhibitor treatment does not
261 directly counter HIF1a activity, but rather circumvents the effect of HIF1a accumulation by
262 increasing oligodendrocyte differentiation despite persistent HIF signaling.

263 Gene set enrichment analysis (GSEA) revealed that AZD8330 treatment of sgVhl OPCs
264 led to an enrichment for “Oligodendrocyte Differentiation” and “Oligodendrocyte Development”
265 pathways, which were normally depleted in sgVhl OPCs compared to control (Figures 5D and
266 5E). Further supporting this, AZD8330 treatment of sgVhl OPCs led to a significant increase in

267 the subset of genes within the GO term “Oligodendrocyte Development, GO:0014003” that were
268 normally decreased in sgVhl OPCs compared to control (fold change of sgVhl to control OPCs
269 <0.75), such as *Sox10* and *Myrf* (Figures 5F and 5G). We validated the AZD8330-mediated
270 increase in expression of both of these transcription factors, which are critical for oligodendrocyte
271 differentiation, by qPCR (Figure 5G). To confirm that this was a function of impaired MEK/ERK
272 signaling, treatment of sgVhl OPCs with ERK1/2 inhibitors AZD0364 and SCH772984 led to a
273 similar increase in *Sox10* expression compared to DMSO (Figure S5B). Collectively, these data
274 suggest that the reduction of *Sox10* expression by cell-type-specific HIF1a targets is critical for
275 the HIF-mediated block in oligodendrocyte differentiation, such that restoration of *Sox10*
276 expression without altering canonical HIF function restores oligodendrocyte formation.
277

278 **MEK/ERK inhibition drives oligodendrocyte formation in hypoxic regions of human**
279 **oligocortical spheroids**

280 In order to ascertain if these mechanisms are conserved in the human context, we leveraged a
281 previously established method of generating human myelinating cortical spheroids from
282 pluripotent stem cells (Madhavan et al., 2018). The interior of human brain spheroids is hypoxic
283 (Brawner et al., 2017; Giandomenico and Lancaster, 2017), and we hypothesized that these
284 hypoxic regions would inhibit oligodendrocyte formation, which could be overcome using a MEK
285 inhibitor. To test this, we treated oligocortical spheroids with either DMSO or 300nM AZD8330 for
286 4 days starting at 70 days *in vitro*, immediately following induction of oligodendrocytes. At day
287 90, spheroids were treated with hypoxyprobe, a chemical used to visualize hypoxic regions less
288 than 1% O_2 (Pogue et al., 2001), and harvested for analysis (Figure 5H). Immunohistochemistry
289 for oligodendrocytes (MYRF+ cells) and hypoxic regions (defined by hypoxyprobe + staining)
290 demonstrated a significant 3.8-fold reduction in the number of MYRF+ oligodendrocytes in
291 hypoxic regions compared to normoxic regions within the spheroids (Figures 5I and 5J).
292 MEK/ERK inhibition with AZD8330 treatment led to a significant 2.3-fold increase in the number

293 of oligodendrocytes within hypoxic regions of the spheroid (Figures 5I and 5J). Collectively these
294 results show that oxygen tensions shape oligodendrocyte development and that MEK inhibition
295 circumvents the hypoxia-mediated inhibition of oligodendrocyte formation in 3D models of human
296 brain development.
297

298 **DISCUSSION**

299 Cells are equipped to translate external cues from the environment into internal signals that
300 ultimately alter transcriptional programs. Molecular oxygen is crucial to support energy production
301 of the cell, and low oxygen upregulates a rapid and conserved transcriptional response mediated
302 largely by HIF transcription factors in all mammalian cells. HIF1a promotes an adaptive response
303 by upregulating oxygen-independent metabolism and increasing blood vessel formation;
304 however, chronic accumulation of HIF1a negatively impacts the function of almost every organ
305 system (Kullmann et al., 2020; Lee et al., 2019; Menendez-Montes et al., 2016; Takubo et al.,
306 2010).

307 Here, we profiled the genome-wide functional targets of HIF1a in OPCs and found that
308 HIF1a not only binds to canonical hypoxia response genes that are shared across multiple cell
309 types, but also activates a unique set of non-canonical genes in a cell-type-specific manner. In
310 the context of the brain, these non-canonical HIF1a targets that impair oligodendrocyte formation
311 could have implications in the numerous hypoxia driven pathologies of white matter such as
312 diffuse white matter injury of prematurity (Salmaso et al., 2014; van Tilborg et al., 2018), white
313 matter stroke in adults (Hankey, 2017; Marin and Carmichael, 2018) and multiple sclerosis
314 (Graumann et al., 2003; Zeis et al., 2008). More broadly, we suggest that non-canonical HIF1a
315 targets in diverse cell types impact a variety of cell-type-specific functions, such as
316 oligodendrocyte differentiation, heart morphogenesis and T-cell activation. This concept has
317 previously been overlooked as many studies have focused on canonical targets of HIF1a or those

that were discovered in immortalized cell lines, which may behave differently in response to HIF1a accumulation.

The same transcription factor can bind to different gene targets in different cell types through interaction with transcriptional machinery unique to each cell type (Mullen et al., 2011; Trompouki et al., 2011). HIF1a binding has been shown to depend on the openness and activation status of chromatin; however, we and others show that chromatin accessibility is not the sole predictor of HIF1a binding (Schodel et al., 2011; Smythies et al., 2019; Xia and Kung, 2009). Our results highlight that HIF1a binds more strongly at core hypoxia response peaks compared to cell-type-specific peaks, which are enriched for open chromatin as well as motifs for lineage-defining transcription factors. This implies that acute HIF1a binds more readily to protective pathways in the immediate response to low oxygen, while chronic HIF1a interacts with lineage defining transcription factors to upregulate targets that ultimately impair development and function in a cell-type-specific manner. These non-canonical targets could represent either a pathological "off-target" effect of sustained HIF1a accumulation or a normal cell-type-specific response to molecular oxygen levels that is coopted in the context of hypoxia disease.

Overall, this work advances our conceptual understanding of the tissue specific response to chronic HIF accumulation and how oxygen tensions regulate tissue physiology and pathology.

ACKNOWLEDGEMENTS

This research was supported by grants from the National Institutes of Health F30HD096784 (K.C.A), T32NS077888 (K.C.A.), and T32GM007250 (K.C.A) and the New York Stem Cell Foundation (P.J.T. and M.A.S.) as well as institutional support from CWRU School of Medicine and philanthropic support from the Enrile, Peterson, Fakhouri, Long, Goodman, Geller, and Weidenthal families. Additional support was provided by the Small Molecule Drug Development and Genomics core facilities of the CWRU Comprehensive Cancer Center (P30CA043703), the CWRU Light Microscopy Imaging Center (S10-OD016164), and the University of Chicago Genomics Facility. The authors thank Brian Popko for tissue samples (obtained with funding from NIH grant R01NS034939). We are also grateful to C. Baecher-Allan, J. LaManna, K. Xu, D. Adams, Y. Federov, L. Barbar, E. Prendergast, E. Schwarz, P. Scacheri, D. Neu, E. Cohn, A. Saiakhova, Z. Nevin, M. Elitt, and R. Sallari for technical assistance and/or discussion.

AUTHOR CONTRIBUTIONS

K.C.A. and P.J.T. conceived and managed the overall study. K.C.A. and L.R.H. performed, quantified and analyzed all *in vitro* experiments using mouse OPCs including qPCR, western blot, immunocytochemistry, and generation of CRISPR knockout and CRISPRA OPCs. K.C.A. performed the small molecule screen and dose curve validations. C.F.B. trained K.C.A. to perform ChIP-seq and K.C.A. performed all ChIP-seq experiments in the paper with analysis of data performed by A.R.M and S.H. A.R.M. and M.A.S. assisted with RNA-seq data analysis. I.R.B. performed mass spectroscopy and quantified the data. B.L.C. generated immunopanned *in vivo* derived OPCs and brain tissue samples. M.M. and A.G. performed oligocortical spheroid experiments. M.A.S. and B.L.C contributed key ideas for experimental design and assembly of figures. K.C.A. assembled all figures and performed statistical analyses. K.C.A. and P.J.T. wrote the manuscript with input from all authors.

DECLARATION OF INTERESTS

P.J.T. is a co-founder and consultant for Convelo therapeutics, which has licensed unrelated patents from Case Western Reserve University. P.J.T and Case Western Reserve University hold equity in Convelo Therapeutics. All other authors have no competing interests.

REFERENCES

Baas, D., Bourbeau, D., Sarlieve, L.L., Ittel, M.E., Dussault, J.H., and Puymirat, J. (1997). Oligodendrocyte maturation and progenitor cell proliferation are independently regulated by thyroid hormone. Glia *19*, 324-332.

Barres, B.A., Hart, I.K., Coles, H.S., Burne, J.F., Voyvodic, J.T., Richardson, W.D., and Raff, M.C. (1992). Cell death and control of cell survival in the oligodendrocyte lineage. Cell *70*, 31-46.

Barres, B.A., Lazar, M.A., and Raff, M.C. (1994). A novel role for thyroid hormone, glucocorticoids and retinoic acid in timing oligodendrocyte development. Development *120*, 1097-1108.

Bartlett, H., Veenstra, G.J., and Weeks, D.L. (2010). Examining the cardiac NK-2 genes in early heart development. Pediatr Cardiol *31*, 335-341.

Brawner, A.T., Xu, R., Liu, D., and Jiang, P. (2017). Generating CNS organoids from human induced pluripotent stem cells for modeling neurological disorders. Int J Physiol Pathophysiol Pharmacol *9*, 101-111.

Cassavaugh, J., and Lounsbury, K.M. (2011). Hypoxia-mediated biological control. J Cell Biochem *112*, 735-744.

Chang, K.J., Redmond, S.A., and Chan, J.R. (2016). Remodeling myelination: implications for mechanisms of neural plasticity. Nat Neurosci *19*, 190-197.

Choudhry, H., and Harris, A.L. (2018). Advances in Hypoxia-Inducible Factor Biology. Cell Metab *27*, 281-298.

Ciofani, M., Madar, A., Galan, C., Sellars, M., Mace, K., Pauli, F., Agarwal, A., Huang, W., Parkhurst, C.N., Muratet, M.*, et al.* (2012). A validated regulatory network for Th17 cell specification. Cell *151*, 289-303.

Clayton, B.L., Huang, A., Dukala, D., Soliven, B., and Popko, B. (2017a). Neonatal Hypoxia Results in Peripheral Nerve Abnormalities. Am J Pathol *187*, 245-251.

392 Clayton, B.L., Huang, A., Kunjamma, R.B., Solanki, A., and Popko, B. (2017b). The integrated stress
393 response in hypoxia-induced diffuse white matter injury. J Neurosci.

394 Creyghton, M.P., Cheng, A.W., Welstead, G.G., Kooistra, T., Carey, B.W., Steine, E.J., Hanna, J.,
395 Lodato, M.A., Frampton, G.M., Sharp, P.A.*, et al.* (2010). Histone H3K27ac separates active from poised
396 enhancers and predicts developmental state. Proc Natl Acad Sci U S A *107*, 21931-21936.

397 Dengler, V.L., Galbraith, M., and Espinosa, J.M. (2014). Transcriptional regulation by hypoxia inducible
398 factors. Crit Rev Biochem Mol Biol *49*, 1-15.

399 Doench, J.G., Fusi, N., Sullender, M., Hegde, M., Vaimberg, E.W., Donovan, K.F., Smith, I., Tothova, Z.,
400 Wilen, C., Orchard, R.*, et al.* (2016). Optimized sgRNA design to maximize activity and minimize off-target
401 effects of CRISPR-Cas9. Nat Biotechnol *34*, 184-191.

402 Emery, B. (2010). Regulation of oligodendrocyte differentiation and myelination. Science *330*, 779-782.

403 Fancy, S.P., Harrington, E.P., Yuen, T.J., Silbereis, J.C., Zhao, C., Baranzini, S.E., Bruce, C.C., Otero,
404 J.J., Huang, E.J., Nusse, R.*, et al.* (2011). Axin2 as regulatory and therapeutic target in newborn brain
405 injury and remyelination. Nat Neurosci *14*, 1009-1016.

406 Gao, F.B., Apperly, J., and Raff, M. (1998). Cell-intrinsic timers and thyroid hormone regulate the
407 probability of cell-cycle withdrawal and differentiation of oligodendrocyte precursor cells. Dev Biol *197*, 54-
408 66.

409 Giandomenico, S.L., and Lancaster, M.A. (2017). Probing human brain evolution and development in
410 organoids. Curr Opin Cell Biol *44*, 36-43.

411 Graumann, U., Reynolds, R., Steck, A.J., and Schaeren-Wiemers, N. (2003). Molecular changes in
412 normal appearing white matter in multiple sclerosis are characteristic of neuroprotective mechanisms
413 against hypoxic insult. Brain Pathol *13*, 554-573.

414 Grinspan, J.B., Edell, E., Carpio, D.F., Beesley, J.S., Lavy, L., Pleasure, D., and Golden, J.A. (2000).
415 Stage-specific effects of bone morphogenetic proteins on the oligodendrocyte lineage. J Neurobiol *43*, 1-
416 17.

417 Guimaraes-Camboa, N., Stowe, J., Aneas, I., Sakabe, N., Cattaneo, P., Henderson, L., Kilberg, M.S.,
418 Johnson, R.S., Chen, J., McCulloch, A.D.*, et al.* (2015). HIF1alpha Represses Cell Stress Pathways to
419 Allow Proliferation of Hypoxic Fetal Cardiomyocytes. Dev Cell *33*, 507-521.

420 Haase, V.H. (2009). The VHL tumor suppressor: master regulator of HIF. Curr Pharm Des *15*, 3895-3903.

421 Hankey, G.J. (2017). Stroke. Lancet *389*, 641-654.

422 Heinz, S., Benner, C., Spann, N., Bertolino, E., Lin, Y.C., Laslo, P., Cheng, J.X., Murre, C., Singh, H., and
423 Glass, C.K. (2010). Simple combinations of lineage-determining transcription factors prime cis-regulatory
424 elements required for macrophage and B cell identities. Mol Cell *38*, 576-589.

425 Horlbeck, M.A., Gilbert, L.A., Villalta, J.E., Adamson, B., Pak, R.A., Chen, Y., Fields, A.P., Park, C.Y.,
426 Corn, J.E., Kampmann, M.*, et al.* (2016). Compact and highly active next-generation libraries for CRISPR-
427 mediated gene repression and activation. Elife *5*.

428 Huang, L.E. (2008). Carrot and stick: HIF-alpha engages c-Myc in hypoxic adaptation. Cell Death Differ
429 *15*, 672-677.

430 Hubler, Z., Allimuthu, D., Bederman, I., Elitt, M.S., Madhavan, M., Allan, K.C., Shick, H.E., Garrison, E.,
431 M, T.K., Factor, D.C.*, et al.* (2018). Accumulation of 8,9-unsaturated sterols drives oligodendrocyte
432 formation and remyelination. Nature *560*, 372-376.

433 Ivan, M., Kondo, K., Yang, H., Kim, W., Valiando, J., Ohh, M., Salic, A., Asara, J.M., Lane, W.S., and
434 Kaelin, W.G., Jr. (2001). HIFalpha targeted for VHL-mediated destruction by proline hydroxylation:
435 implications for O2 sensing. Science *292*, 464-468.

436 Jaakkola, P., Mole, D.R., Tian, Y.M., Wilson, M.I., Gielbert, J., Gaskell, S.J., von Kriegsheim, A.,
437 Hebestreit, H.F., Mukherji, M., Schofield, C.J.*, et al.* (2001). Targeting of HIF-alpha to the von Hippel-
438 Lindau ubiquitylation complex by O2-regulated prolyl hydroxylation. Science *292*, 468-472.

439 Jablonska, B., Gierdalski, M., Chew, L.J., Hawley, T., Catron, M., Lichauco, A., Cabrera-Luque, J., Yuen,
440 T., Rowitch, D., and Gallo, V. (2016). Sirt1 regulates glial progenitor proliferation and regeneration in
441 white matter after neonatal brain injury. Nat Commun *7*, 13866.

442 Jablonska, B., Scafidi, J., Aguirre, A., Vaccarino, F., Nguyen, V., Borok, E., Horvath, T.L., Rowitch, D.H.,
443 and Gallo, V. (2012). Oligodendrocyte regeneration after neonatal hypoxia requires FoxO1-mediated
444 p27Kip1 expression. J Neurosci *32*, 14775-14793.

445 Joung, J., Konermann, S., Gootenberg, J.S., Abudayyeh, O.O., Platt, R.J., Brigham, M.D., Sanjana, N.E.,
446 and Zhang, F. (2017). Genome-scale CRISPR-Cas9 knockout and transcriptional activation screening.
447 Nat Protoc *12*, 828-863.

448 Kaelin, W.G., Jr., and Ratcliffe, P.J. (2008). Oxygen sensing by metazoans: the central role of the HIF
449 hydroxylase pathway. Mol Cell *30*, 393-402.

450 Kaluz, S., Kaluzova, M., and Stanbridge, E.J. (2003). Expression of the hypoxia marker carbonic
451 anhydrase IX is critically dependent on SP1 activity. Identification of a novel type of hypoxia-responsive
452 enhancer. Cancer Res *63*, 917-922.

453 Kullmann, J.A., Trivedi, N., Howell, D., Laumonnerie, C., Nguyen, V., Banerjee, S.S., Stabley, D.R.,
454 Shirinifard, A., Rowitch, D.H., and Solecki, D.J. (2020). Oxygen Tension and the VHL-Hif1alpha Pathway
455 Determine Onset of Neuronal Polarization and Cerebellar Germinal Zone Exit. Neuron.

456 Kupferschmidt, K. (2019). Cellular oxygen sensor system earns Nobel for trio. Science *366*, 167.

457 Lager, A.M., Corradin, O.G., Cregg, J.M., Elitt, M.S., Shick, H.E., Clayton, B.L.L., Allan, K.C., Olsen, H.E.,
458 Madhavan, M., and Tesar, P.J. (2018). Rapid functional genetics of the oligodendrocyte lineage using
459 pluripotent stem cells. Nat Commun *9*, 3708.

460 Lee, J.W., Ko, J., Ju, C., and Eltzschig, H.K. (2019). Hypoxia signaling in human diseases and
461 therapeutic targets. Exp Mol Med *51*, 68.

462 Lee, Y.S., Kim, J.W., Osborne, O., Oh, D.Y., Sasik, R., Schenk, S., Chen, A., Chung, H., Murphy, A.,
463 Watkins, S.M.*, et al.* (2014). Increased adipocyte O2 consumption triggers HIF-1alpha, causing
464 inflammation and insulin resistance in obesity. Cell *157*, 1339-1352.

465 Levy, C., Khaled, M., and Fisher, D.E. (2006). MITF: master regulator of melanocyte development and
466 melanoma oncogene. Trends Mol Med *12*, 406-414.

467 Liddelow, S.A., Guttenplan, K.A., Clarke, L.E., Bennett, F.C., Bohlen, C.J., Schirmer, L., Bennett, M.L.,
468 Munch, A.E., Chung, W.S., Peterson, T.C.*, et al.* (2017). Neurotoxic reactive astrocytes are induced by
469 activated microglia. Nature *541*, 481-487.

470 Loftus, S.K., Baxter, L.L., Cronin, J.C., Fufa, T.D., Program, N.C.S., and Pavan, W.J. (2017). Hypoxia-
471 induced HIF1alpha targets in melanocytes reveal a molecular profile associated with poor melanoma
472 prognosis. Pigment Cell Melanoma Res *30*, 339-352.

473 Madhavan, M., Nevin, Z.S., Shick, H.E., Garrison, E., Clarkson-Paredes, C., Karl, M., Clayton, B.L.L.,
474 Factor, D.C., Allan, K.C., Barbar, L.*, et al.* (2018). Induction of myelinating oligodendrocytes in human
475 cortical spheroids. Nature methods *15*, 700-706.

476 Majmundar, A.J., Wong, W.J., and Simon, M.C. (2010). Hypoxia-inducible factors and the response to
477 hypoxic stress. Mol Cell *40*, 294-309.

478 Marin, M.A., and Carmichael, S.T. (2018). Mechanisms of demyelination and remyelination in the young
479 and aged brain following white matter stroke. Neurobiol Dis.

480 Mei, F., Fancy, S.P.J., Shen, Y.A., Niu, J., Zhao, C., Presley, B., Miao, E., Lee, S., Mayoral, S.R.,
481 Redmond, S.A.*, et al.* (2014). Micropillar arrays as a high-throughput screening platform for therapeutics
482 in multiple sclerosis. Nat Med *20*, 954-960.

483 Menendez-Montes, I., Escobar, B., Palacios, B., Gomez, M.J., Izquierdo-Garcia, J.L., Flores, L., Jimenez-
484 Borreguero, L.J., Aragones, J., Ruiz-Cabello, J., Torres, M.*, et al.* (2016). Myocardial VHL-HIF Signaling
485 Controls an Embryonic Metabolic Switch Essential for Cardiac Maturation. Dev Cell *39*, 724-739.

486 Miska, J., Lee-Chang, C., Rashidi, A., Muroski, M.E., Chang, A.L., Lopez-Rosas, A., Zhang, P., Panek,
487 W.K., Cordero, A., Han, Y.*, et al.* (2019). HIF-1alpha Is a Metabolic Switch between Glycolytic-Driven
488 Migration and Oxidative Phosphorylation-Driven Immunosuppression of Tregs in Glioblastoma. Cell Rep
489 *27*, 226-237 e224.

490 Mullen, A.C., Orlando, D.A., Newman, J.J., Loven, J., Kumar, R.M., Bilodeau, S., Reddy, J., Guenther,
491 M.G., DeKoter, R.P., and Young, R.A. (2011). Master transcription factors determine cell-type-specific
492 responses to TGF-beta signaling. Cell *147*, 565-576.

493 Nagao, A., Kobayashi, M., Koyasu, S., Chow, C.C.T., and Harada, H. (2019). HIF-1-Dependent
494 Reprogramming of Glucose Metabolic Pathway of Cancer Cells and Its Therapeutic Significance. Int J
495 Mol Sci *20*.

496 Najm, F.J., Madhavan, M., Zaremba, A., Shick, E., Karl, R.T., Factor, D.C., Miller, T.E., Nevin, Z.S.,
497 Kantor, C., Sargent, A.*, et al.* (2015). Drug-based modulation of endogenous stem cells promotes
498 functional remyelination in vivo. Nature *522*, 216-220.

499 Najm, F.J., Zaremba, A., Caprariello, A.V., Nayak, S., Freundt, E.C., Scacheri, P.C., Miller, R.H., and
500 Tesar, P.J. (2011). Rapid and robust generation of functional oligodendrocyte progenitor cells from
501 epiblast stem cells. Nature methods *8*, 957-962.

502 Nave, K.A. (2010). Myelination and the trophic support of long axons. Nat Rev Neurosci *11*, 275-283.

503 Pogue, B.W., Paulsen, K.D., O'Hara, J.A., Wilmot, C.M., and Swartz, H.M. (2001). Estimation of oxygen
504 distribution in RIF-1 tumors by diffusion model-based interpretation of pimonidazole hypoxia and
505 eppendorf measurements. Radiat Res *155*, 15-25.

506 Quinlan, A.R., and Hall, I.M. (2010). BEDTools: a flexible suite of utilities for comparing genomic features.
507 Bioinformatics *26*, 841-842.

508 Ramirez, F., Ryan, D.P., Gruning, B., Bhardwaj, V., Kilpert, F., Richter, A.S., Heyne, S., Dundar, F., and
509 Manke, T. (2016). deepTools2: a next generation web server for deep-sequencing data analysis. Nucleic
510 Acids Res *44*, W160-165.

511 Rechsteiner, M.P., von Teichman, A., Nowicka, A., Sulser, T., Schraml, P., and Moch, H. (2011). VHL
512 gene mutations and their effects on hypoxia inducible factor HIFalpha: identification of potential driver and
513 passenger mutations. Cancer Res *71*, 5500-5511.

514 Salmaso, N., Jablonska, B., Scafidi, J., Vaccarino, F.M., and Gallo, V. (2014). Neurobiology of premature
515 brain injury. Nat Neurosci *17*, 341-346.

516 Sanjana, N.E., Shalem, O., and Zhang, F. (2014). Improved vectors and genome-wide libraries for
517 CRISPR screening. Nature methods *11*, 783-784.

518 Scafidi, J., Hammond, T.R., Scafidi, S., Ritter, J., Jablonska, B., Roncal, M., Szigeti-Buck, K., Coman, D.,
519 Huang, Y., McCarter, R.J., Jr*., et al.* (2014). Intranasal epidermal growth factor treatment rescues
520 neonatal brain injury. Nature *506*, 230-234.

521 Schmid-Burgk, J.L., Schmidt, T., Gaidt, M.M., Pelka, K., Latz, E., Ebert, T.S., and Hornung, V. (2014).
522 OutKnocker: a web tool for rapid and simple genotyping of designer nuclease edited cell lines. Genome
523 Res *24*, 1719-1723.

524 Schmidt, D., Wilson, M.D., Spyrou, C., Brown, G.D., Hadfield, J., and Odom, D.T. (2009). ChIP-seq: using
525 high-throughput sequencing to discover protein-DNA interactions. Methods *48*, 240-248.

526 Schodel, J., Oikonomopoulos, S., Ragoussis, J., Pugh, C.W., Ratcliffe, P.J., and Mole, D.R. (2011). High-
527 resolution genome-wide mapping of HIF-binding sites by ChIP-seq. Blood *117*, e207-217.

528 Semenza, G.L. (2007). Life with oxygen. Science *318*, 62-64.

529 Semenza, G.L. (2012). Hypoxia-inducible factors in physiology and medicine. Cell *148*, 399-408.

530 Shaul, Y.D., and Seger, R. (2007). The MEK/ERK cascade: from signaling specificity to diverse functions.
531 Biochim Biophys Acta *1773*, 1213-1226.

532 Shindo, A., Liang, A.C., Maki, T., Miyamoto, N., Tomimoto, H., Lo, E.H., and Arai, K. (2016). Subcortical
533 ischemic vascular disease: Roles of oligodendrocyte function in experimental models of subcortical white-
534 matter injury. J Cereb Blood Flow Metab *36*, 187-198.

535 Smythies, J.A., Sun, M., Masson, N., Salama, R., Simpson, P.D., Murray, E., Neumann, V., Cockman,
536 M.E., Choudhry, H., Ratcliffe, P.J*., et al.* (2019). Inherent DNA-binding specificities of the HIF-1alpha and
537 HIF-2alpha transcription factors in chromatin. EMBO Rep *20*.

538 Stolt, C.C., Lommes, P., Friedrich, R.P., and Wegner, M. (2004). Transcription factors Sox8 and Sox10
539 perform non-equivalent roles during oligodendrocyte development despite functional redundancy.
540 Development *131*, 2349-2358.

541 Stolt, C.C., Rehberg, S., Ader, M., Lommes, P., Riethmacher, D., Schachner, M., Bartsch, U., and
542 Wegner, M. (2002). Terminal differentiation of myelin-forming oligodendrocytes depends on the
543 transcription factor Sox10. Genes Dev *16*, 165-170.

544 Tabula Muris, C., Overall, c., Logistical, c., Organ, c., processing, Library, p., sequencing, Computational
545 data, a., Cell type, a., Writing, g*., et al.* (2018). Single-cell transcriptomics of 20 mouse organs creates a
546 Tabula Muris. Nature *562*, 367-372.

547 Takubo, K., Goda, N., Yamada, W., Iriuchishima, H., Ikeda, E., Kubota, Y., Shima, H., Johnson, R.S.,
548 Hirao, A., Suematsu, M*., et al.* (2010). Regulation of the HIF-1alpha level is essential for hematopoietic
549 stem cells. Cell Stem Cell *7*, 391-402.

550 Trompouki, E., Bowman, T.V., Lawton, L.N., Fan, Z.P., Wu, D.C., DiBiase, A., Martin, C.S., Cech, J.N.,
551 Sessa, A.K., Leblanc, J.L.*, et al.* (2011). Lineage regulators direct BMP and Wnt pathways to cell-specific
552 programs during differentiation and regeneration. Cell *147*, 577-589.

553 van Tilborg, E., de Theije, C.G.M., van Hal, M., Wagenaar, N., de Vries, L.S., Benders, M.J., Rowitch,
554 D.H., and Nijboer, C.H. (2018). Origin and dynamics of oligodendrocytes in the developing brain:
555 Implications for perinatal white matter injury. Glia *66*, 221-238.

556 Volpe, J.J. (2009). Brain injury in premature infants: a complex amalgam of destructive and
557 developmental disturbances. Lancet Neurol *8*, 110-124.

558 Volpe, J.J., Kinney, H.C., Jensen, F.E., and Rosenberg, P.A. (2011). The developing oligodendrocyte:
559 key cellular target in brain injury in the premature infant. Int J Dev Neurosci *29*, 423-440.

560 Wu, Y., Tang, D., Liu, N., Xiong, W., Huang, H., Li, Y., Ma, Z., Zhao, H., Chen, P., Qi, X.*, et al.* (2017).
561 Reciprocal Regulation between the Circadian Clock and Hypoxia Signaling at the Genome Level in
562 Mammals. Cell Metab *25*, 73-85.

563 Xia, X., and Kung, A.L. (2009). Preferential binding of HIF-1 to transcriptionally active loci determines cell-
564 type specific response to hypoxia. Genome Biol *10*, R113.

565 Yohe, M.E., Gryder, B.E., Shern, J.F., Song, Y.K., Chou, H.C., Sindiri, S., Mendoza, A., Patidar, R.,
566 Zhang, X., Guha, R.*, et al.* (2018). MEK inhibition induces MYOG and remodels super-enhancers in RAS-
567 driven rhabdomyosarcoma. Sci Transl Med *10*.

568 Yu, Y., Chen, Y., Kim, B., Wang, H., Zhao, C., He, X., Liu, L., Liu, W., Wu, L.M., Mao, M.*, et al.* (2013).
569 Olig2 targets chromatin remodelers to enhancers to initiate oligodendrocyte differentiation. Cell *152*, 248-
570 261.

571 Yuen, T.J., Silbereis, J.C., Griveau, A., Chang, S.M., Daneman, R., Fancy, S.P., Zahed, H., Maltepe, E.,
572 and Rowitch, D.H. (2014). Oligodendrocyte-encoded HIF function couples postnatal myelination and
573 white matter angiogenesis. Cell *158*, 383-396.

574 Zeis, T., Graumann, U., Reynolds, R., and Schaeren-Wiemers, N. (2008). Normal-appearing white matter
575 in multiple sclerosis is in a subtle balance between inflammation and neuroprotection. Brain *131*, 288-
576 303.

577 Zhang, S., Kim, B., Zhu, X., Gui, X., Wang, Y., Lan, Z., Prabhu, P., Fond, K., Wang, A., and Guo, F.
578 (2020). Glial type specific regulation of CNS angiogenesis by HIFα-activated different signaling pathways.
579 bioRxiv, 2020.2001.2031.929661.

580 Zhang, Y., Chen, K., Sloan, S.A., Bennett, M.L., Scholze, A.R., O'Keeffe, S., Phatnani, H.P., Guarnieri,
581 P., Caneda, C., Ruderisch, N.*, et al.* (2014). An RNA-sequencing transcriptome and splicing database of
582 glia, neurons, and vascular cells of the cerebral cortex. J Neurosci *34*, 11929-11947.

583 **METHODS**

584

585 **OPC preparation and culture**

586 OPCs were generated from the epiblast stem cells (EpiSCs) as previously described (Najm et al.,
587 2011). These EpiSC derived OPCs were sorted to purity by fluorescence activated cell sorting
588 using conjugated CD140a-APC (eBioscience, 17-1401; 1:80) and NG2-AF488 (Millipore,
589 AB5320A4; 1:100) antibodies. Primary mouse OPCs were derived using two methods. In the first
590 method, cerebral cortices were harvested from postnatal day 2 (P2) C57BL/6J pups and
591 dissociated using a Tumor Dissociation Kit (Miltenyi). Cells were then filtered through a 70 µm
592 filter, washed in DMEM/F12, and plated on poly-ornithine (PO) (Sigma, P3655-50MG) and laminin
593 (Sigma, L2020-1MG) coated plates to be expanded, passaged, and used in experiments. The
594 second method follows the immunopanning protocol from P7 C57BL/6J mice (Barres et al., 1992).
595 Primary *in vivo* derived OPCs using either method were pooled from multiple pups such that they
596 are a combination of male and female cells.

597 All OPCs were grown on PO and laminin coated flasks in growth media consisting of
598 DMEM/F12 supplemented with N2 Max (R&D Systems), B27 (Thermo Fisher), 20ng/mL bFGF
599 (R&D Systems), and 20ng/mL PDGFA (R&D Systems). Media was changed every 48 hours.

600

601 **Mouse OPC differentiation to oligodendrocytes and astrocytes**

602 For oligodendrocyte generation, OPCs were seeded at either 40,000 cells per well (96-well plate,
603 Fisher, 167008) or 15,000 cells per well (384-well PDL-coated cell carrier plates, PerkinElmer,
604 6057500) on plates coated with PO and laminin. Oligodendrocyte differentiation media consisted
605 of DMEM/F12 supplemented with N2 Max, B27, 100ng/mL noggin (R&D, 3344NG050), 100ng/mL
606 IGF-1 (R&D, 291G1200), 10uM cyclic AMP (Sigma, D0260-100MG), 10ng/mL NT3 (R&D,
607 267N3025) and 40ng/mL T3 (Thyroid hormone, Sigma, T-6397). Cells were analyzed after 3 days
608 unless otherwise noted.

609 For OPC differentiation to astrocytes, 30,000 OPCs were plated per well in a 96 well plate
610 (Fisher, 167008) containing astrocyte differentiation media described in (Liddelow et al., 2017).
611 This media consisted of a 1:1 (v/v) mixture of neurobasal media and high glucose DMEM
612 supplemented with sodium pyruvate, glutamax, N2 Max, and N-acetyl-cysteine and with growth
613 factors including 20ng/mL bFGF, 5ng/mL Hb-EGF (R&D, 259-HE-050), 10ng/mL CNTF (R&D,
614 557-NT-010), and 10ng/mL BMP4 (R&D, 314-BP-050) for 3 days.
615

616 ***In vitro* hypoxia experiments**

617 OPCs were plated in OPC growth media and then placed into a 2 shelf C-Chamber from
618 BioSpherix (C-274). Oxygen tension was controlled using the ProOx 110 from BioSpherix such
619 that nitrogen gas would flush out oxygen to maintain the chamber at the desired oxygen level.
620 The subchamber was set at 1% O_2 and cells were cultured for 48 hours unless otherwise noted.
621 Hypoxia treated cells were then rapidly lysed for RNA or protein to minimize degradation of HIFs
622 upon exposure to room air. The normoxic controls were cultured concurrently in the same cell
623 culture incubator containing the BioSpherix C-chamber.
624

625 **Immunocytochemistry**

626 For antigens requiring live staining (O1 and O4), antibodies were diluted in N2B27 base media
627 supplemented with 10% Donkey Serum (v/v) (017-000-121, Jackson ImmunoResearch) and then
628 added to cells for 18 minutes at 37°C. Cells were then fixed in cold 4% PFA (Electron microscopy
629 sciences) for 18 minutes at room temperature, washed with PBS, and permeabilized and blocked
630 in blocking solution containing 0.1% Triton X-100 in PBS supplemented with 10% normal donkey
631 serum (v/v) for 30 minutes at room temperature. Primary antibodies were diluted in blocking
632 solution and incubated with samples overnight at 4°C. Primary antibodies used included anti-
633 OLIG2 (1.2µg/mL, Proteintech, 12999-1-AP), anti-MBP (1:100, Abcam, ab7349), anti-O1 (1:50,
634 CCF Hybridoma Core), anti-O4 (1:100, CCF Hybridoma Core), anti-ASCL2 (1:10, EMD Millipore,

635 MAB4417), and anti-GFAP (1:5,000, Dako, Z033401-2). The next day, cells were rinsed with PBS
636 and incubated in blocking solution for one hour with the appropriate secondary antibody
637 conjugated to an Alexa-Fluor (4ug/mL, Thermo Fisher) along with the nuclear stain DAPI (Sigma,
638 1ug/mL).
639

640 **High content imaging and quantification**

641 Both 96-well and 384-well plates were imaged using the Operetta High Content imaging and
642 analysis system (PerkinElmer). For 96-well and 384-well plates, 8 fields and 5-fields were
643 captured from each well at 20x magnification respectively. Images were analyzed with
644 PerkinElmer Harmony and Columbus software as described previously (Hubler et al., 2018; Najm
645 et al., 2015). In brief, nuclei of live cells were identified using a threshold for area of DAPI staining
646 to exclude pyknotic nuclei or debris. To identify oligodendrocytes, each DAPI positive nucleus
647 was expanded by 50% to determine potential intersection with staining of an oligodendrocyte
648 marker (O4/O1/MBP) in a separate channel. Expanded nuclei that intersected O4/O1/MBP
649 staining were scored as oligodendrocytes. Percentage of oligodendrocytes was then calculated
650 by dividing the number of oligodendrocytes by total number of DAPI positive cells per image.
651

652 **Generation of CRISPRKO/ CRISPRA OPCs**

653 Guide sequences were curated from the Brie library (Doench et al., 2016) and cloned into the
654 CRISPRv2 backbone (Addgene 52961) (Sanjana et al., 2014) for generating CRISPR-mediated
655 knockout OPCs. Guide sequences were curated from the CRISPRav2 library (Horlbeck et al.,
656 2016) and cloned into the lenti-SAMv2 backbone (Addgene 75112) (Joung et al., 2017) for
657 CRISPR activation. The activation helper plasmid (Addgene 89308) (Joung et al., 2017) was co-
658 transduced for all CRISPR activation OPCs. Plasmids containing cloning sites for the sgRNA
659 were digested and annealed oligomers containing the sgRNA (indicated in the chart below) were
660 then ligated to their respective backbones. Positive bacterial clones were confirmed to have the

661 correct inserted oligomer using Sanger sequencing. HEK293T cells were then transfected using
662 lenti-X shots following the manufacturer's protocol (Clonetech). The next day, transfection media
663 was switched to OPC growth media without growth factors for virus collection. After 2 days, the
664 media from transfected HEK293T cells was collected, filtered, and supplemented with OPC
665 growth factors PDGF and FGF. This lentivirus-containing media was added to OPCs at a ratio of
666 1:2 (v/v) with fresh OPC growth media. After 24 hours of incubation with virus, transduced cells
667 were switched to fresh OPC growth media and allowed to recover for 48 hours. OPCs were then
668 selected for 96 hours in OPC growth media supplemented with a lethal dose of puromycin
669 (500ng/mL, Invitrogen) for CRISPR knockout cells or a lethal dose of blasticidin (10µg/mL,
670 Thermo Fisher, A1113903) and hygromycin (100µg/mL, Thermo Fisher, 10687010) for CRISPR
671 activation cells. OPCs were then allowed to recover for at least 24 hours following removal of
672 selection and frozen down in aliquots for future use. For all experiments, the lentivirally transduced
673 CRISPR/CRISPRA targeting and non-targeting control OPCs were derived from the same batch
674 of OPCs and infected and selected simultaneously. qPCR was performed to validate a reduction
675 or overexpression of gene targets of interest for each batch of CRISPR/CRISPRA OPCs
676 generated.

OPC CRISPR ID	**sgRNA sequence (5' to 3')**
Cas9 control	empty
sgVhl	GCCCGGTGGTAAGATCGGGT
sgVhl.2	TGTCCATCGACATTGAGGGA
CRISPRA-NTC	GATCGGTTATGTTTAGGGTT
CRISPRA-Ascl2	CCAAGTTTACCAGCTTTACG
CRISPRA-Dlx3	GTTAGGGGTAACAACAAAGA
CRISPRA-Vegfa	GAGGCCGTGGACCCTGGTAA
CRISPRA-Slc16a3	GCCTGGCCGCTGTTCCCCGA

677

678 **Validating CRISPR knockout in OPCs**

679 Primers were identified surrounding the target cut site for the two sgVhl constructs (see previous
680 section for sgRNAs) that generate 200-250 base pair amplicons.

681 For the sgVhl cut site the primers were:

682 F 5' TCCCTACACGACGCTCTTCCGATCTCTCTCAGGTCATCTTCTGCAACC 3'

683 R 5' AGTTCAGACGTGTGCTCTTCCGATCTGACAAGATGCTCGGGGTCGG 3'

684 For the sgVhl.2 cut site the primers were:

685 F 5' TCCCTACACGACGCTCTTCCGATCTAATAAACAGGTGCCATGCCC 3'

686 R 5' AGTTCAGACGTGTGCTCTTCCGATCTAGATTGACTATTAACCTGGCAATG 3'

687

688 PCR products were run on an agarose gel, excised by gel extraction (28115, Qiagen), and
689 submitted to the Case Western Reserve University Genomics core for library preparation and
690 sequencing. Libraries were prepared by adding unique indices by PCR using KAPA HiFi HotStart
691 ReadyMix. Samples were then pooled evenly, quantified using NEBNext® Library Quant Kit for
692 Illumina® (E7630, New England 641 Biolabs), and denatured and diluted per Illumina's MiSeq
693 instructions. These finished libraries were then sequenced using an Illumina MiSeq (250bp
694 paired-end). Results were analyzed using Outknocker software (Schmid-Burgk et al., 2014)
695 (http://www.outknocker.org/outknocker2.htm) to calculate the percentage of reads with insertions
696 or deletions at the sgRNA target site.

697

698 **Compound screening and assessment**

699 Compound screening was carried out as described in (Lager et al., 2018). Poly-D-lysine-coated
700 384-well CellCarrier Ultra plates (PerkinElmer) were coated with laminin diluted in N2B27 base
701 media using an EL406 Microplate Washer Dispenser (BioTek) equipped with a 5µl dispense
702 cassette (BioTek) and were incubated at 37ºC for at least 1 hour. A 3mM stock of the Selleck
703 bioactive library in dimethylsulfoxide (DMSO) was then added to the plates using a 50nL solid pin
704 tool attached to a Janus automated workstation (Perkin Elmer) at a 1:1000 dilution such that each
705 well received a single compound at a final concentration of 3µM. Compounds for dose response
706 validation were sourced from the Selleck library, except for ERK1/2 inhibitors SCH772984

707 (Selleck, S7101), AZD0364 (Selleck, S8708), and VX-11e (Selleck, S7709) which were
708 purchased separately. OPCs were dispensed in oligodendrocyte differentiation media at 12,500
709 cells per well into the laminin-coated 384 well plates using the BioTek EL406 Microplate Washer
710 Dispenser and differentiated at 37ºC for 3 days. At this point, cells were fixed, washed and stained
711 using the BioTek EL406 Microplate Washer Dispenser. Cells were stained with anti-MBP (1:100,
712 Abcam, ab7349) along with DAPI (1 µg/ml, Sigma) and imaged using the Operetta High Content
713 Imaging and Analysis system (PerkinElmer).
714
715 **Western blot**
716 For cell culture derived protein samples, at least 1 million OPCs were collected and lysed in RIPA
717 buffer (Sigma) supplemented with protease and phosphatase inhibitor (78441, Thermo Fisher)
718 for at least 15 minutes and cleared by centrifugation at 13,000g at 4ºC for 15 minutes. Protein
719 concentrations were determined using the Bradford assay (Bio-Rad Laboratories). Protein was
720 then diluted and added to Laemmli loading buffer, boiled at 95ºC for 5 minutes, run using NuPAGE
721 Bis-Tris gels (NP0335BOX, Thermo Fisher), and then transferred to PVDF membranes (LC2002,
722 Thermo Fisher). Blocking and primary/secondary antibody solutions were performed for at least
723 30 min with 5% nonfat drug milk (Nestle Carnation) in TBS plus 0.1% Tween 20 (TBST). Primary
724 antibodies used included anti-HIF1a (1:500, Abcam, ab2185), anti-phospho-p44/42 (ERK1/2)
725 (100ng/mL, CST, 9101), anti-p44/42 (total ERK1/2) (100ng/mL, CST, 4696), anti-DLX3 (2µg/mL,
726 abcam, ab178428), anti-SOX10 (1:100, R&D, AF2864), anti-B-Actin peroxidase (1:50,000,
727 Sigma, A3854), anti-VHL (5µg/mL, BD Biosciences, 556347), anti-ASCL2 (1:10, EMD Millipore,
728 MAB4417), anti-MBP (1µg/mL, Biolegend, 808401), and anti-MAG (1µg/mL, Thermo Fisher,
729 346200). Membranes were then imaged using the LI-COR (Odyssey) and analyzed using Image
730 Studio™ software that is integrated into the LI-COR imaging suite. Westerns were normalized to
731 loading control Beta-Actin unless otherwise noted.
732

733 **qRT-PCR**

734 At least 500,000 OPCs were lysed in TRIzol (Ambion) followed by phenol-chloroform extraction
735 and processing with the RNeasy Mini Kit (74104, Qiagen). RNA quality and quantity was
736 determined using a NanoDrop spectrophotometer. cDNA was generated using the iSCRIPT kit
737 following the manufacturer's instructions (1708891, Biorad). qRT-PCR was performed using pre-
738 designed TaqMan gene expression assays (Thermo Fisher). Probe cat numbers and IDs are
739 included in the chart below. qPCR was performed using the Applied Biosystems 7300 real-time
740 PCR system and probes were normalized to *Rpl13a* endogenous control.

Gene ID	Taqman cat. number
Sox10	Mm00569909_m1
Rpl13a	Mm05910660_g1
Vhl	Mm00494137_m1
Ascl2	Mm01268891_g1
Tpi1	Mm00833691_g1
Ciart	Mm01255905_g1
P4ha2	Mm00477940_m1
Pdk1	Mm00554300_m1
Pfkl	Mm00435587_m1
Slc16a3	Mm00446102_m1
Dlx3	Mm00438428_m1
Vefga	Mm00437306_m1
Bnip3	Mm01275600_g1
Pdgfra	Mm00440701_m1
Plp1	Mm01297210_m1
Myrf	Mm01194959_m1

741

742 **RNA-seq sample preparation and analysis**

743 At least 1 million OPCs were lysed in TRIzol and RNA was isolated as described for qPCR.
744 Libraries were prepared following protocols from NEBNext Poly(A) mRNA Magnetic Isolation
745 Module (NEB #E7490L) and NEBNext Ultra RNA Library Prep Kit for Illumina (NEB# E7530L). In
746 brief, samples were enriched for mRNA using oligo(dT) beads, which were then fragmented
747 randomly and used for cDNA generation and subsequent second-strand synthesis using a custom
748 second-strand synthesis buffer (Illumina), dNTPs, RNase H and DNA polymerase I. cDNA

749 libraries then went through terminal repair, A-base ligation, adapter ligation, size selection and
750 PCR enrichment. Final libraries were pooled evenly and sequenced on the Illumina NovaSeq
751 with paired-end 150bp reads with a read-depth of at least 20 million reads per sample.

752 For gene expression analysis, reads were aligned to the mm10 genome build using
753 salmon 0.14.1 (https://github.com/COMBINE-lab/salmon) to quantify transcript abundance in
754 transcripts per million (TPM) values. Transcripts were summarized as gene-level TPM
755 abundances with tximport. A gene with TPM>1 was considered expressed. Differential
756 expression analysis was then performed using DESEQ2
757 (https://bioconductor.org/packages/release/bioc/html/DESeq2.html). Significant genes were
758 called based on p-adj and fold change values as described in the results section.
759

760 **Gene ontology analysis and heatmaps**

761 Metascape (http://metascape.org/) was used to identify significant pathways from RNAseq data.
762 Identification of critical oligodendrocyte genes that were dysregulated in VHL knockout OPCs (see
763 Figure 3A) was performed by fitting RNA-seq (TPM) to the list of genes under the GO term
764 "Oligodendrocyte Development" (GO: 0014003). This spreadsheet of TPM values was used to
765 make a heatmap using the R-package "pheatmap." Increased genes were those greater than 1.25
766 fold change whereas decreased genes were those less than 0.75 fold change in sgVhl relative to
767 Cas9 control OPCs. In Figure 5D and 5E, RNA-seq data was fit to the genes within
768 "Oligodendrocyte Development" (GO: 0014003) that were downregulated in sgVhl OPCs
769 compared to Cas9 control OPCs (fold change less than 0.75).
770

771 **Gene set enrichment analysis**

772 Gene set enrichment analysis (GSEA) scores were generated for gene sets in C5.bp datasets
773 using classic scoring, 1000 gene-set permutations, and signal-to-noise metrics. Normalized

774 enrichment scores, false discovery rate and FWER o-values were all calculated by GSEA
775 software (https://www.gsea-msigdb.org/gsea/index.jsp).

776

777 **ChIP-seq and analysis**

778 Nuclei isolation and chromatin shearing were performed using the Covaris TruChIP protocol
779 following manufacturer's instructions for the "high-cell" format. In brief, 5-20 million cells
780 (H3K27Ac) or 100 million cells (HIF1a) were crosslinked in "Fixing buffer A" supplemented with
781 1% fresh formaldehyde for 10 minutes at room temperature with oscillation and quenched for 5
782 minutes with "Quench buffer E." These cells were then washed with PBS and either snap frozen
783 and stored at -80ºC, or immediately used for nuclei extraction and shearing per the manufacturer
784 protocol. The samples were sonicated with the Covaris S2 using the following settings: 5% Duty
785 factor 4 intensity for four 60-second cycles. Sheared chromatin was cleared and incubated
786 overnight at 4 degrees with primary antibodies that were pre-incubated with protein G magnetic
787 DynaBeads (Thermo Fisher). Primary antibodies used included anti-H3K27Ac (9ug/sample,
788 Abcam, ab4729) and anti-HIF1a (25ug/sample, Abcam, ab2185). These beads were then
789 washed, eluted, reverse cross-linked and treated with RNase A followed by proteinase K. ChIP
790 DNA was purified using Ampure XP beads (Aline Biosciences, C-1003-5) and then used to
791 prepare Illumina sequencing libraries as described previously (Schmidt et al., 2009). Libraries
792 were sequenced on the Illumina HiSeq2500 with single-end 50bp reads with a read-depth of at
793 least 20 million reads per sample.

794 For peak calling, reads were quality and adapter trimmed using Trim Galore! Version
795 0.4.1. Trimmed reads were aligned to mm10 with Bowtie2 version 2.3.2. Duplicate reads (potential
796 artifacts of PCR in library preparation) were removed using Picard MarkDuplicates. Peaks were
797 called with MACS version 2.1.1 to define broad peaks for histone marks (H3K27Ac) and narrow
798 peaks for transcription factors (HIF1a) and normalized to background genomic DNA with matched

799 inputs. Thresholding was set at FDR<0.001 for calling both H3K27Ac and HIF1a peaks. Peaks
800 were visualized with the Integrative Genomics Viewer (IGV, Broad Institute). Peaks were assigned
801 to the nearest expressed gene (TPM>1 in Cas9 control or sgVhl OPCs) using bedtools available
802 in Galaxy (https://usegalaxy.org).
803
804 **Diffbind analysis**
805 H3K27Ac ChIP-seq was performed in duplicate from two independent batches of Cas9 control
806 and sgVhl OPCs. Differential H3K27Ac analysis between sgVhl and Cas9 control OPCs was
807 performed using "Diffbind software"
808 (https://bioconductor.org/packages/release/bioc/html/DiffBind.html). A false discovery rate of 0.1
809 was used to call significantly enriched and depleted regions of H3K27Ac.
810
811 **Motif enrichment analysis**
812 Motifs were called under significant HIF1a peaks (FDR<0.001) or regions of significantly gained
813 H3K27Ac (FDR<0.1) using HOMERv4.11.1 (Heinz et al., 2010). The FindMotifsGenome.pl tool
814 was used with 1000bp windows with mm10 as the reference genome.
815
816 **HIF1a ChIP-seq overlap analysis**
817 HIF1a ChIP-seq raw data were re-analyzed for: two HIF1a replicates ChIP-seqs and 1 input of
818 E12.5 heart (GSM1500750, GSM1500751, GSM1500749) (Guimaraes-Camboa et al., 2015), two
819 HIF1a replicates ChIP-seqs and 1 input of melanocyte (GSM2305570, GSM2305571,
820 GSM2305572) (Loftus et al., 2017), and two HIF1a ChIP-seqs and 2 inputs of Th17 cells
821 (GSM1004819, GSM1004991, GSM1004820, GSM1004993) (Ciofani et al., 2012). For each of
822 the HIF1a ChIP-seqs, the peaks were called as described above (MACS2, narrow peak,
823 FDR<0.001). Peaks unique to OPCs were identified by finding peaks not found in the union of all
824 the replicates of every other tissue sample using the bedtools (v 2.25.0) (Quinlan and Hall, 2010)

825 "intersect" command. Common peaks across tissues were also identified using the bedtools
826 "intersect". RPCG-normed bigwigs were used to create aggregate plots for HIF1a, ATAC-seq,
827 and H3K27ac using the deeptools (version 3.3.1) (Ramirez et al., 2016) "computeMatrix" and
828 “plotHeatmap” commands, centering on the HIF1a peak locations in the sgVhl OPCs. Genes
829 within 5Kb of these HIF1a peaks were called as HIF1a target genes. For melanocytes and T-cells,
830 HIF1a target genes were called as only those at the intersection of both of the available replicates.
831 For embryonic heart there were fewer peaks called compared to the other tissues, so HIF1a gene
832 targets were called as the union of the two available replicates. These gene and peak lists were
833 used to generate venn diagrams using the following webtool:
834 (http://bioinformatics.psb.ugent.be/webtools/Venn/). Cell type specific gene targets of HIF1a were
835 called if the gene was only a target of HIF1a in that specific cell type.
836

837 **Mass spectrometry for lactate and pyruvate**

838 OPCs were cultured in OPC growth media and after growth media was removed, cells were
839 washed with ice-cold saline (3 times) and collected with 1 ml of 80% ethanol pre-chilled on dry
840 ice. Cells were frozen at -80ºC until analyses. This cell extract was then vortexed and sonicated
841 for 30 seconds on, 30 seconds off, alternating for 10 minutes. Next, cells were pelleted by
842 centrifugation at 4°C for 10 min at 14,000 rpm. Supernatant was transferred to GC/MS vials and
843 evaporated to dryness under gentle stream of nitrogen. Keto- and aldehyde groups were reduced
844 by addition of 10 µl of 1 N NaOH plus 15 µl NaB^2H_4 (prepared as 10 mg/ml in 50 mM NaOH).
845 After mixing, samples were incubated at room temperature for 1 hour and then acidified by 55 µl
846 of 1 N HCl by dropping the acid slowly. Next, samples were evaporated to dryness. Next, 50 µl of
847 methanol were added to precipitate boric acid. Internal standard was added (10 µl of 17:0 FA, 0.1
848 mg/ml). Samples were evaporated to dryness and reacted with 40 µl of pyridine and 60 µl of tert-
849 butylbis(dimethylsilyl) trifluoroacetamide with 10% trimethylchlorosilane (Regisil) TBDMS at 60°C
850 for 1 hour. Resulting TBDMS derivatives were injected into GC/MS. Analyses were then carried

851 out on an Agilent 5973 mass spectrometer equipped with 6890 Gas Chromatograph. A HP-5MS
852 capillary column (60 m × 0.25 mm × 0.25 μm) was used in all assays with a helium flow of 1
853 ml/min. Samples were analyzed in Selected Ion Monitoring (SIM) mode using electron impact
854 ionization (EI). Ion dwell time was set to 10 msec. Lactate and pyruvate were both measured for
855 all samples.
856
857 **Tissue from mild chronic hypoxia (MCH) mice**
858 MCH is a well described model of Diffuse White Matter Injury (DWMI) (Clayton et al., 2017a;
859 Clayton et al., 2017b; Fancy et al., 2011; Scafidi et al., 2014; Yuen et al., 2014) and protein
860 samples were generously provided by Brian Popko. In brief, postnatal day 3 (P3) C57Bl6 pups
861 were placed into a BioSpherix chamber maintained at 10+/- 0.5% O2 by displacement of nitrogen
862 until P11. Animals were then quickly sacrificed by CO_2 asphyxiation followed by decapitation and
863 the frontal cortex was isolated as this region has been shown to contain subcortical white matter
864 that is susceptible to hypoxia-induced DWMI (Clayton et al., 2017b; Jablonska et al., 2012;
865 Sanjana et al., 2014; Yuen et al., 2014).
866
867 **Oligocortical spheroid generation and immunohistochemistry**
868 Human embryonic stem cells (line H7, WiCell) were grown in mTesR1 media and oligocortical
869 spheroids were generated as previously described (Madhavan et al., 2018). Spheroids were
870 treated every other day with DMSO or 300nM AZD8330 between days 70 and 74 and harvested
871 on day 90. 2 hours prior to harvesting, spheroids were treated with 200uM Hypoxyprobe-1
872 (pimonidazole, Hypoxyprobe Inc, Burlington MA). Spheroids were washed in PBS and fixed
873 overnight in ice cold 4% Paraformaldehyde and then washed in PBS and cryoprotected in a 30%
874 sucrose solution. Spheroids were frozen in OCT and sectioned at thickness of 15 μm. Slides
875 were washed in PBS and incubated overnight with anti-MyRF (1:1000, gift from Michael Wegner)
876 and anti-pimonidazole antibodies (1:250, Hypoxyprobe Inc, Burlington MA) followed by labelling

877 with appropriate Alexa-Fluor labeled secondary antibodies (2μg/mL, Thermo Fisher). Images
878 were captured using a Hamamatsu Nanozoomer S60 Slide scanner with NDP 2.0 software.
879 Images spanning the edge to the central region of each oligocortical spheroid were used for
880 analysis. MyRF+ oligodendrocytes in Hypoxyprobe+ and Hypoxyprobe- areas within each image
881 were quantified using ImageJ software.
882

883 **Statistics and replicates**

884 GraphPad Prism was used to perform statistical analyses unless otherwise noted. Statistical tests
885 and replicate descriptions are detailed in each figure legend. In brief, black filled-in circles for bar
886 graphs indicate biological replicates whereas open circles represent technical replicates.
887 Statistics were only performed on samples with biological replicates. Data is typically graphed as
888 mean ± standard deviation (SD) or ± standard error of the mean (SEM) as detailed in the figure
889 legend. A p-value less than 0.05 was considered significant unless otherwise noted.

890 **FIGURE 1**

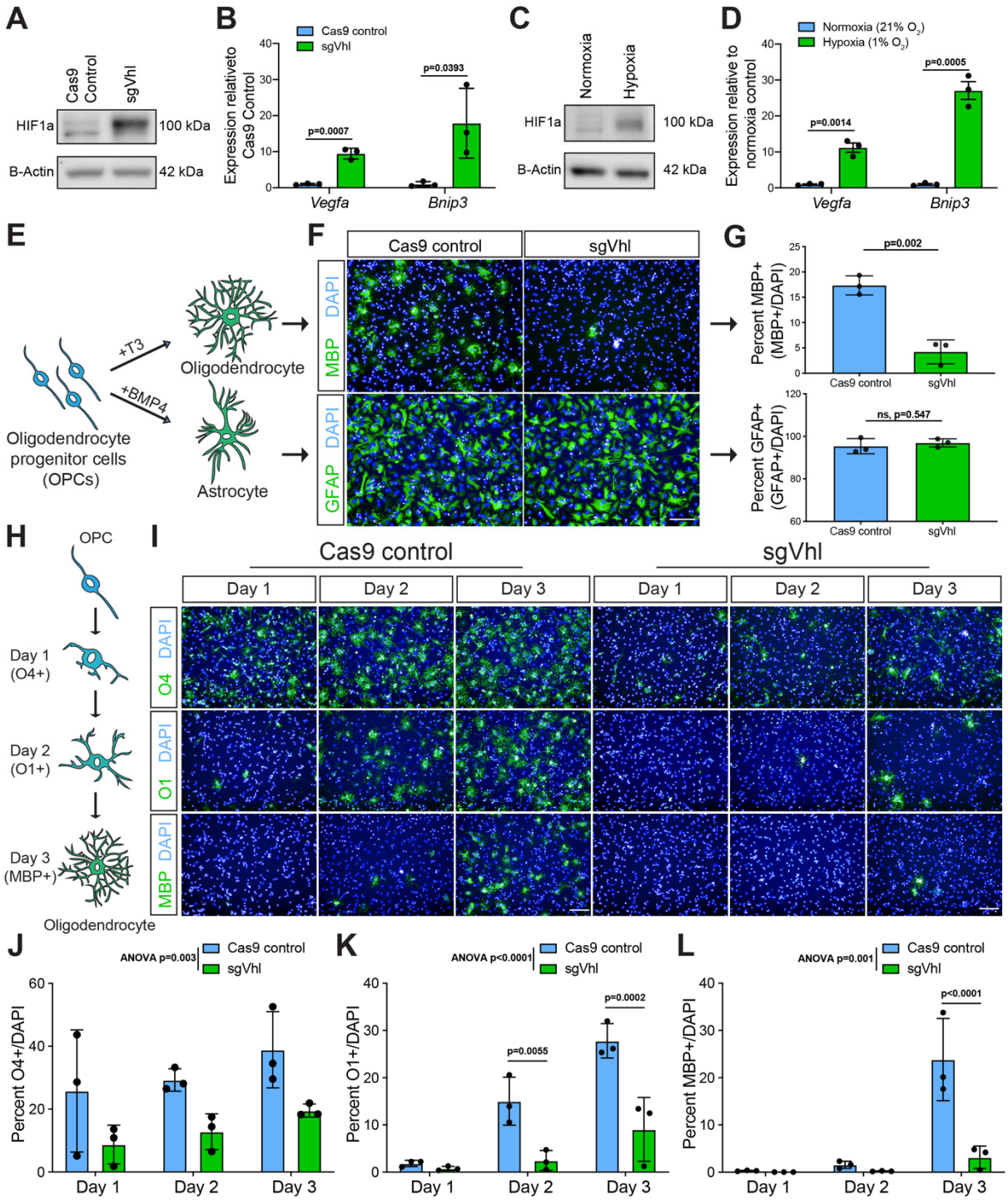

891

892 **Figure 1. HIF1a Accumulation Impairs the Induction of Oligodendrocytes from OPCs**

893 **(A)** Western blot of HIF1a from nuclear lysates of sgVhl OPCs compared to Cas9 control OPCs
894 with B-Actin as a loading control. Molecular weight is indicated to the right of the blot.

895 **(B)** qRT-PCR of HIF target genes *Vegfa* and *Bnip3* in Cas9 control (in blue) and sgVhl (in green)
896 OPCs normalized to endogenous loading control *Rpl13a*. Data are presented as mean ± SEM
897 from 3 independent biological replicates (experiments) with 4 technical replicates (individual wells)
898 per experiment. p-values were calculated using Student's two-tailed t-test.

899 **(C)** Western blot of HIF1a from nuclear lysates of OPCs cultured in hypoxia (1% O_2) compared to
900 normoxia (21% O_2) with B-Actin as a loading control. Molecular weight is indicated to the right of
901 the blot.

902 **(D)** qRT-PCR of HIF target genes *Vegfa* and *Bnip3* in OPCs cultured in physiological hypoxia (in
903 green) compared to normoxia (in blue) normalized to endogenous loading control *Rpl13a*. Data
904 are presented as mean ± SEM from 3 independent biological replicates (experiments) with 4
905 technical replicates (individual wells) per experiment. p-values were calculated using Student's
906 two-tailed t-test.

907 **(E)** Schematic of the two *in vitro* differentiation schemes directing OPCs to either oligodendrocytes
908 through addition of thyroid hormone (T3) or astrocytes through the addition of BMP4.

909 **(F)** Representative images of Cas9 control and sgVhl oligodendrocytes (MBP+ in green) and
910 astrocytes (GFAP+ in green) following 3 days in the respective differentiation media. Nuclei are
911 marked by DAPI (in blue). Scale bar, 100μm.

912 **(G)** Quantification of the percentage of oligodendrocytes (MBP+ cells / DAPI) and astrocytes
913 (GFAP+ cells / DAPI) formed from sgVhl OPCs (in green) compared to Cas9 control OPCs (in
914 blue). Data are presented as mean ± SD from 3 independent biological replicates (experiments)
915 with 6-8 technical replicates (individual wells) per experiment. p-values were calculated using
916 Student's two-tailed t-test.

917 **(H)** Schematic illustrating acquisition of early (O4), intermediate (O1) and late (MBP)
918 oligodendrocyte markers during the 3-day *in vitro* oligodendrocyte differentiation procedure in
919 response to addition of T3.

920 **(I)** Representative images of early (O4+ in green), intermediate (O1+ in green) and late (MBP+ in
921 green) oligodendrocytes during days 1, 2, and 3 of differentiation with Cas9 control and sgVhl
922 OPCs. Nuclei are marked by DAPI (in blue). Scale bars, 100μm.

923 **(J-L)** Quantification of the percentage of early O4+ (J), intermediate O1+ (K), and late MBP+ (L)
924 oligodendrocytes in sgVhl OPCs (in green) compared to Cas9 control OPCs (in blue) at days 1,
925 2, and 3 of differentiation. Data are presented as mean ± SD from 3 independent biological
926 replicates (experiments) with 6-8 technical replicates (individual wells) per experiment. To analyze
927 overall differences between Cas9 control and sgVhl OPCs across all timepoints, p-values were
928 calculated using two-way ANOVA (reported as ANOVA p=). To test differences between Cas9
929 control and sgVhl OPCs at individual timepoints, p-values were calculated using Sidak's multiple
930 comparisons test.

931 See also Figure S1.

FIGURE S1

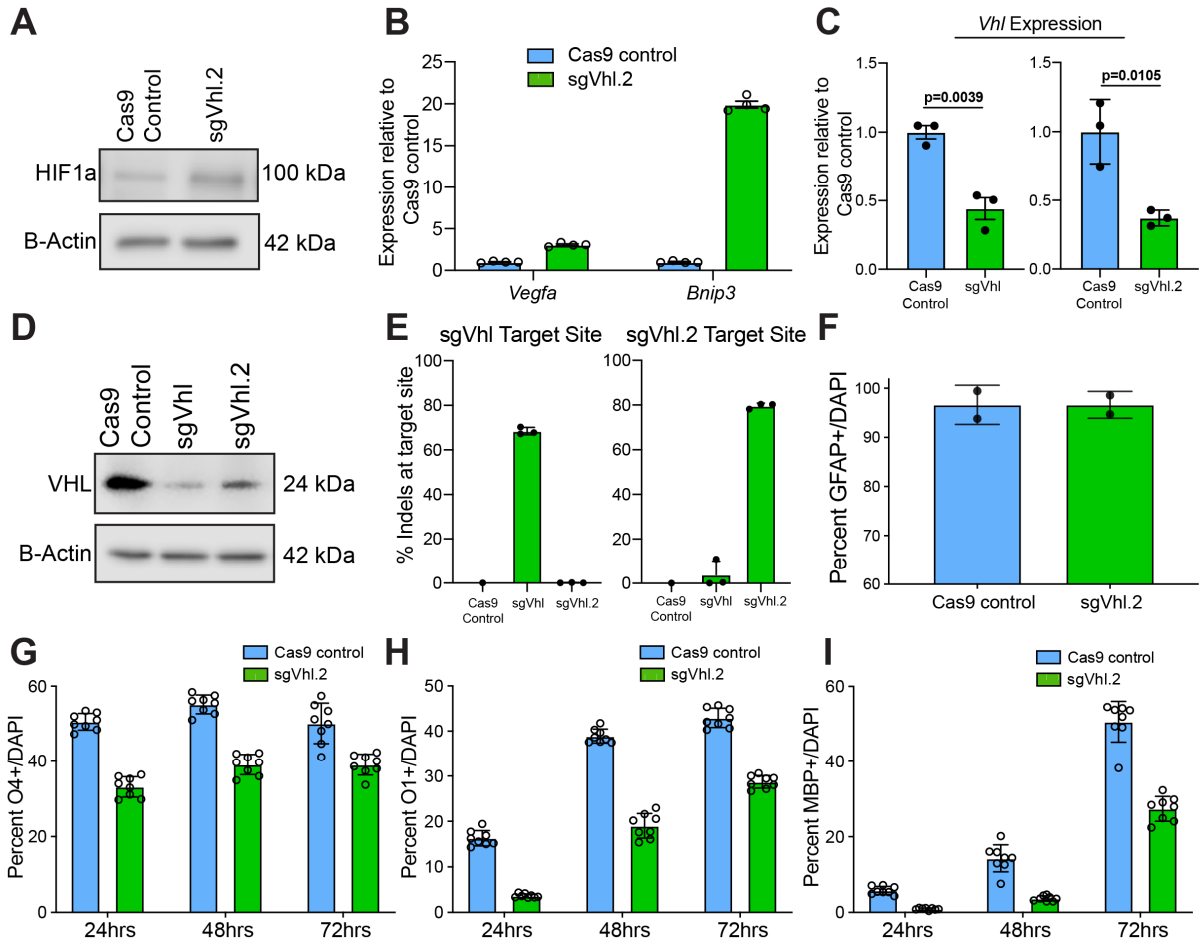

Figure S1. CRISPR Mediated Knockout of Vhl Leads to Loss of *Vhl* Expression and Impairs Oligodendrocyte Formation, Related to Figure 1.

(A) Western blot of HIF1a from nuclear lysates of sgVhl.2 OPCs compared to Cas9 control OPCs with B-Actin as a loading control. Molecular weight is indicated to the right of the blot.

(B) qRT-PCR of HIF target genes *Vegfa* and *Bnip3* in sgVhl.2 OPCs (in green) compared to Cas9 control OPCs (in blue) normalized to endogenous loading control *Rpl13a*. Data are presented as mean ± SEM from 4 technical replicates (individual wells).

(C) qRT-PCR of *Vhl* in both sgVhl and sgVhl.2 OPCs (both in green) compared to Cas9 control OPCs (in blue) normalized to endogenous loading control *Rpl13a*. Data are presented as mean ± SEM from 3 independent biological replicates (experiments) with 4 technical replicates (individual wells) per experiment. p-values were calculated using Student's two-tailed t-test.

(D) Western blot of VHL from whole cell lysate of sgVhl and sgVhl.2 OPCs compared to Cas9 control OPCs with B-Actin as a loading control. Molecular weight is indicated to the right of the blot.

948 **(E)** In-del analysis utilizing Outknocker software on PCR products surrounding sgRNA cut sites
949 for both sgVhl and sgVhl.2 OPCs compared to Cas9 control. Data are presented as mean ± SD
950 from 3 independent biological replicates (experiments).

951 **(F)** Quantification of the percentage of astrocytes (GFAP+ cells/ DAPI) formed from sgVhl.2 OPCs
952 (in green) compared to Cas9 control OPCs (in blue). Data are presented as mean ± SD from 2
953 independent biological replicates (experiments) with 6-8 technical replicates (individual wells) per
954 experiment.

955 **(G-I)** Quantification of the percentage of early O4+ (G), intermediate O1+ (H), and late MBP+ (I)
956 oligodendrocytes formed from sgVhl.2 OPCs (in green) compared to Cas9 control OPCs (in blue)
957 at day 1, 2 and 3 of differentiation. Data are presented as mean ± SD from 8 technical replicates
958 (individual wells) per condition.

FIGURE 2

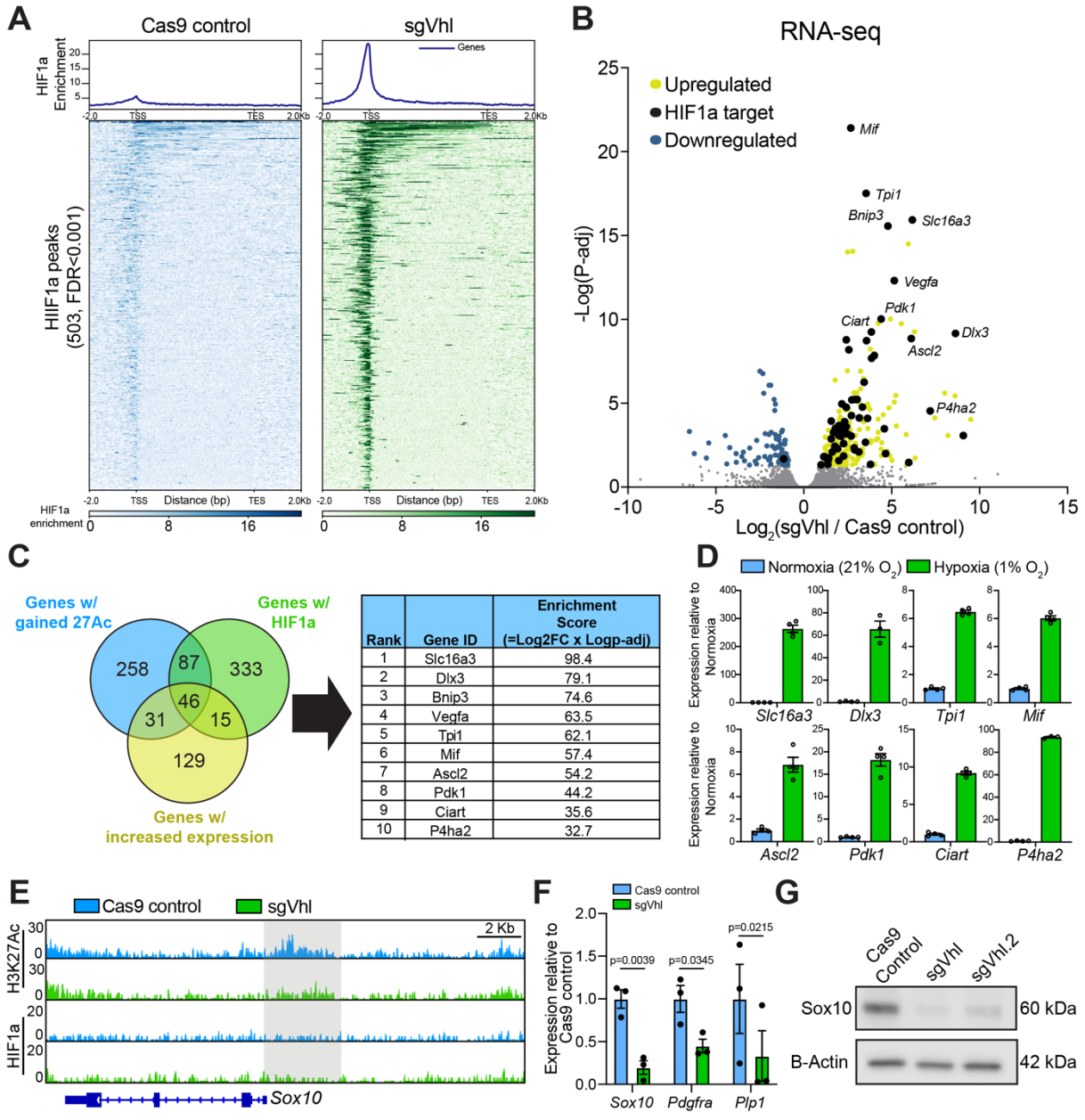

Rank	Gene ID	Enrichment Score (=Log2FC x Logp-adj)
1	Slc16a3	98.4
2	Dlx3	79.1
3	Bnip3	74.6
4	Vegfa	63.5
5	Tpi1	62.1
6	Mif	57.4
7	Ascl2	54.2
8	Pdk1	44.2
9	Ciart	35.6
10	P4ha2	32.7

Figure 2. HIF1a Accumulation Suppresses Sox10 Expression

(A) Aggregate binding profile and heatmap of the 503 HIF1a peaks called by MACS2 (narrow peaks, FDR<0.001) in sgVhl OPCs within 2Kb of the transcription start site (TSS) and transcription end site (TES) of the closest expressed gene in both Cas9 control and sgVhl OPCs normalized to input.

(B) Volcano plot of genes that significantly increase (in yellow) and decrease (in blue) with direct targets of HIF1a in black in sgVhl compared to Cas9 control OPCs (p-adj <0.05). Gray dots are genes not significantly different between conditions. Genes indicated in italics represent examples of top direct HIF1a targets in OPCs. Data are from 3 biological replicates (independent samples).

970 **(C)** Venn diagram highlighting top functional HIF1a targets in OPCs by overlapping genes with
971 proximal HIF1a binding (FDR<0.001, in green), significant gains in H3K27ac (FDR<0.1, in blue)
972 and significantly increased expression (P-adj<0.05, in purple). Genes were then ranked by their
973 enrichment score, which is the product of the Log_2(Fold change in gene expression) and -Log(P-
974 adj). The top 10 targets are displayed in the table ranked by their respective enrichment scores.

975 **(D)** qRT-PCR of 8 top HIF1a target genes (see Figure 1D for *Vegfa* and *Bnip3*) in OPCs treated
976 with hypoxia (1% O_2, in green) compared to normoxia (21% O_2, in blue) normalized to
977 endogenous loading control *Rpl13a*. Data are presented as mean ± SEM from 3-4 technical
978 replicates (individual wells) per condition.

979 **(E)** Genome browser view of H3K27ac and HIF1a signals in Cas9 control (in blue) and sgVhl (in
980 green) OPCs normalized to input at the locus for *Sox10* with a reduction in H3K27ac proximal to
981 the *Sox10* promoter highlighted in gray. Scale bar, 2Kb.

982 **(F)** qRT-PCR of *Sox10* and downstream Sox10 target genes *Pdgfra* and *Plp1* in sgVhl OPCs (in
983 green) compared to Cas9 control OPCs (in blue) normalized to endogenous loading control
984 *Rpl13a*. Data are presented as mean ± SEM from 3 biological replicates (independent
985 experiments) with 3-4 technical replicates (individual wells) per experiment. p-values were
986 calculated using Student's two-tailed t-test.

987 **(G)** Western blot of nuclear lysates for SOX10 in sgVhl and Vhl.2 OPCs compared to Cas9 control
988 OPCs relative to B-Actin loading control. Molecular weight is indicated to the right of the blot.

989 See also Figure S2.

990 **FIGURE S2**

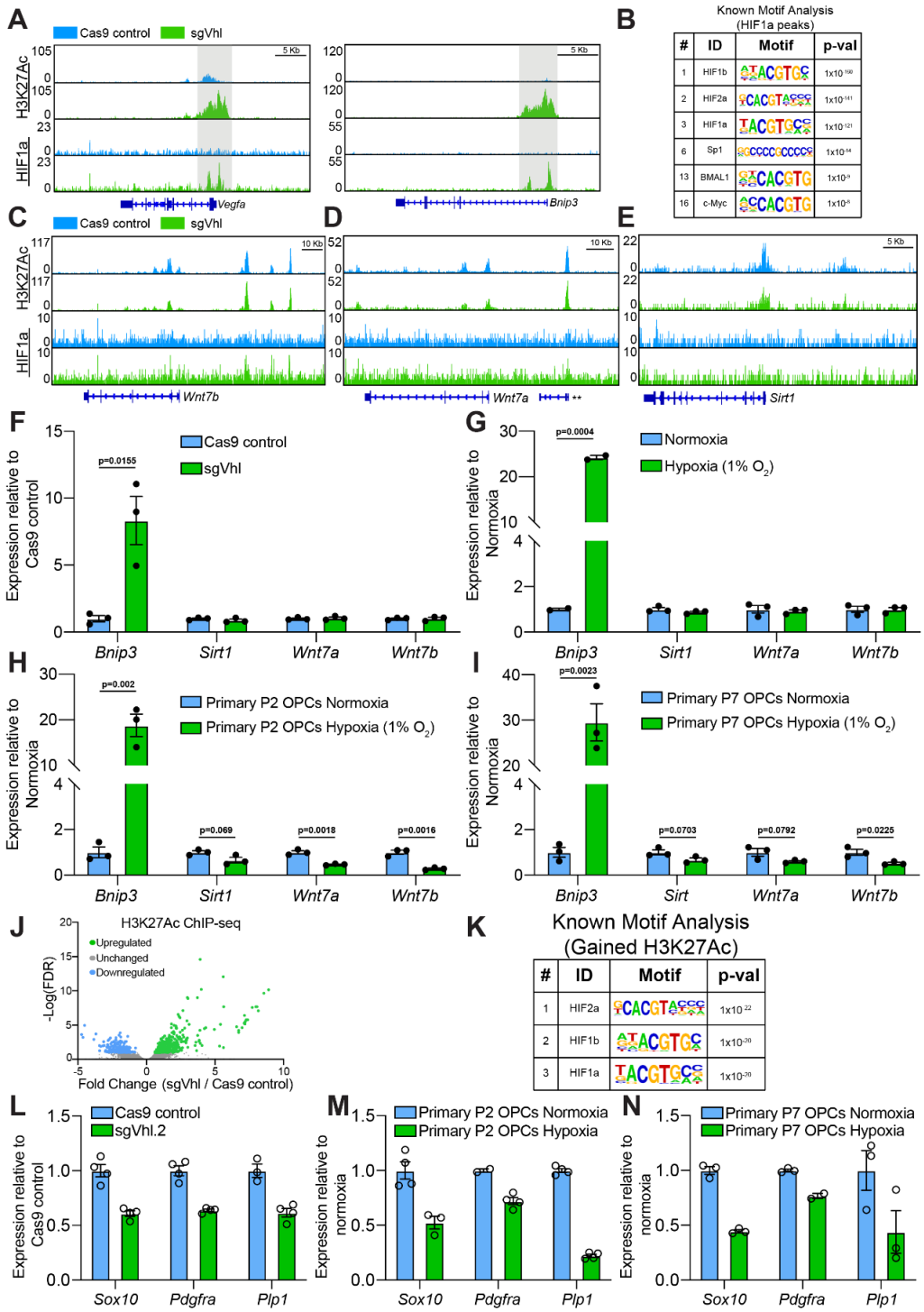

991

992 **Figure S2. HIF1a Accumulation Suppresses Sox10 Expression, Related to Figure 2.**

993 **(A)** Genome browser view of H3K27ac and HIF1a signals in Cas9 control (in blue) and sgVhl (in
994 green) OPCs normalized to input at the locus for *Vegfa* and *Bnip3*. HIF1a and active chromatin
995 accumulation in sgVhl OPCs are highlighted in gray. Scale bars, 5Kb.

996 **(B)** Table of known motifs significantly enriched in HIF1a peaks in sgVhl OPCs (FDR<0.001)
997 displaying the transcription factor name, motif, and p-value ranked in order of significance (#
998 indicates rank out of all motifs from the analysis).

999 **(C-E)** H3K27ac and HIF1a ChIP-seq in Cas9 control (in blue) and sgVhl (in green) OPCs
1000 normalized to input at the locus for *Wnt7b*. Scale bars, 10Kb (C-D) and 5Kb (E). ** is
1001 4930471M09Rik.

1002 **(F-I)** qRT-PCR of *Bnip3*, *Sirt1, Wnt7a* or *Wnt7b* in Cas9 control OPCs (in blue) and sgVhl OPCs
1003 (in green) (F), OPCs treated with normoxia (in blue) or hypoxia (1% O_2, in green) (G), primary
1004 postnatal day 2 (P2) *in vivo* derived mouse OPCs cultured in physiological hypoxia (1% O_2, in
1005 green) compared to normoxia (in blue) (H), and primary immunopanned postnatal day 7 (P7) *in*
1006 *vivo* derived mouse OPCs cultured in physiological hypoxia (1% O_2, in green) compared to
1007 normoxia (in blue) (I) normalized to endogenous loading control *Rpl13a*. Data are presented as
1008 mean ± SEM from 3 independent biological replicates (experiments) with 4 technical replicates
1009 (individual wells) per experiment. p-values were calculated using Student's two-tailed t-test.**J)**
1010 Volcano plot of fold change in intensity of H3K27ac peaks (FDR<0.001) between Cas9 control
1011 and sgVhl OPCs showing regions of significantly increased H3K27ac (FDR<0.1, in green) and
1012 decreased H3K27ac (FDR<0.1, in blue).

1013 **(J)** Volcano plot of fold change in intensity of significant H3K27ac regions (FDR<0.001) between
1014 Cas9 control and sgVhl OPCs showing regions of significantly increased H3K27ac (FDR<0.1, in
1015 green) and decreased H3K27ac (FDR<0.1, in blue).

1016 **(K)** Table of known motifs in regions significantly enriched for H3K27ac (FDR<0.1) in sgVhl OPCs
1017 compared to Cas9 control OPCs displaying the transcription factor name, motif, and p-value
1018 ranked in order of significance (# indicates rank out of all motifs from the analysis).

1019 **(L-N)** qRT-PCR of *Sox10* and downstream Sox10 target genes *Pdgfra* and *Plp1* in sgVhl.2 (in
1020 green) compared to Cas9 control OPCs (in blue) (L), in primary postnatal day 2 (P2) *in vivo*
1021 derived mouse OPCs treated with physiological hypoxia (in green) compared to normoxia (in blue)
1022 (M), and in primary immunopanned postnatal day 7 (P7) *in vivo* derived mouse OPCs treated with
1023 physiological hypoxia (in green) compared to normoxia (in blue) (N). All qRT-PCRs are
1024 normalized to endogenous loading control *Rpl13a*. Data are presented as mean ± SEM from 3-4
1025 technical replicates (individual wells) per condition.

1026 **FIGURE 3**

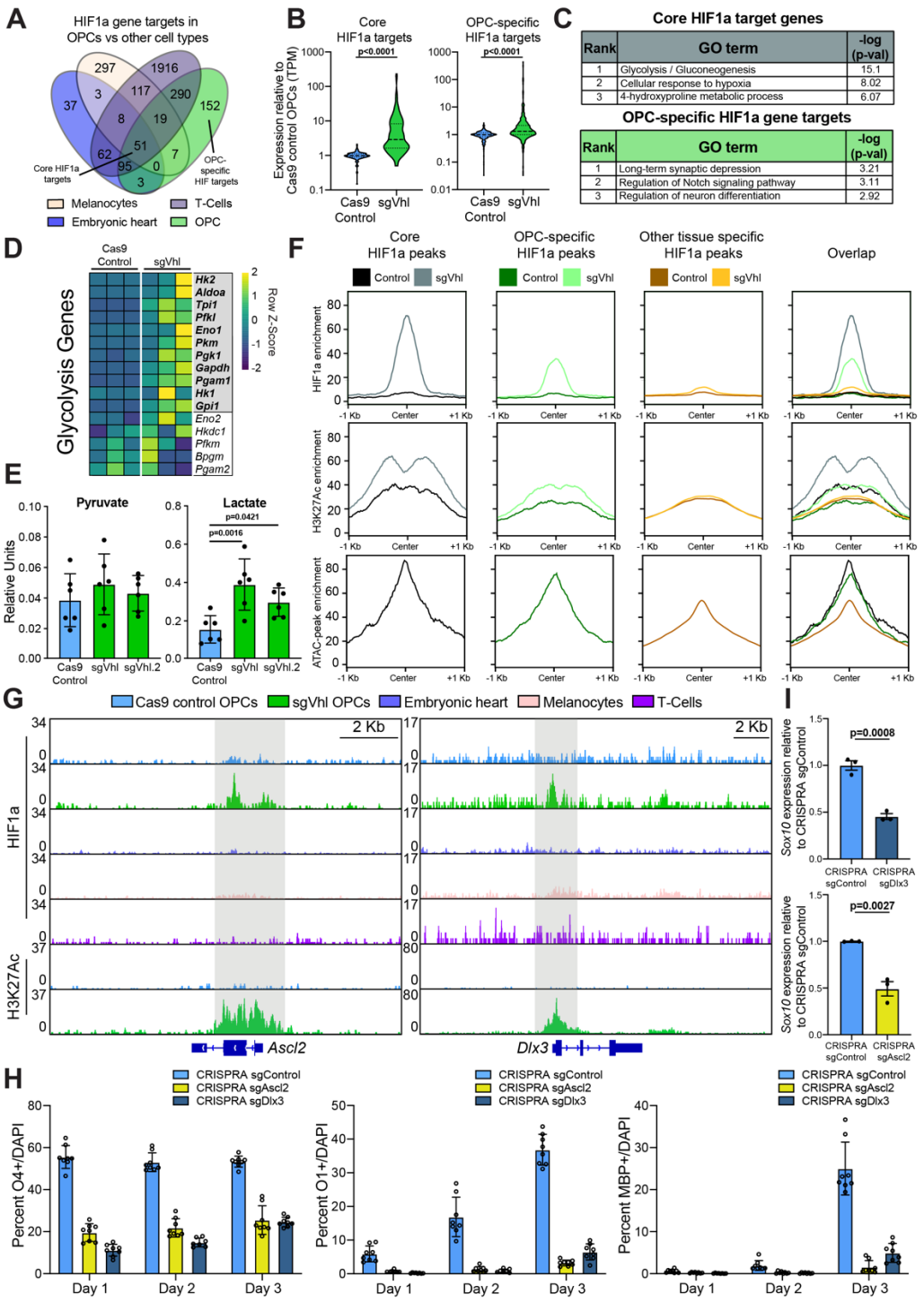

1027

1028 **Figure 3. Ectopic Expression of OPC-specific HIF1a Targets Downregulates Sox10 and**
1029 **Impairs Oligodendrocyte Differentiation**

1030 **(A)** Venn diagram of direct HIF1a target genes from publicly available HIF1a ChIP-seq datasets
1031 in diverse mouse tissues overlapped with HIF1a targets in OPCs (using MACS2, narrowpeaks,
1032 FDR<0.001, limited to genes within 5Kb of significant HIF1a peaks).

1033 **(B)** Violin plots of compiled expression data (TPM) normalized to Cas9 control OPCs for genes in
1034 core and OPC-specific HIF1a target categories in Cas9 control (in blue) and sgVhl (in green).
1035 Bold dashed line represents the median with the thin dashed lines representing the upper and
1036 lower quartiles. p-values were calculated using Mann Whitney two-tailed t-test.

1037 **(C)** Gene ontology (GO) analysis of genes that are core targets of HIF1a in all 4 tissue types as
1038 well as genes that are targets of HIF1a specifically in OPCs. Table shows the rank of the GO term
1039 along with –log(p-value).

1040 **(D)** Heatmap of row normalized expression of genes in the glycolysis pathway between Cas9
1041 control and sgVhl OPCs. Genes with their names bolded and in the gray box are direct targets of
1042 HIF1a and exhibit increased expression in OPCs.

1043 **(E)** Targeted metabolomics for pyruvate and lactate in both sgVhl and sgVhl.2 OPCs (both in
1044 green) compared to Cas9 control OPCs (in blue). Data are presented in relative units as mean ±
1045 SD from 6 biological replicates (independent experiments) with one technical replicate (individual
1046 well) per experiment. p-values were calculated using one-way ANOVA with Dunnett's multiple
1047 comparisons test.

1048 **(F)** Aggregate plots of HIF1a and H3K27ac enrichment in Cas9 control and sgVhl OPCs as well
1049 as open chromatin (defined by ATAC-seq) enrichment in normal, non-transduced OPCs at core
1050 HIF1a peaks shared by all 4 tissue types, OPC-specific HIF1a peaks, and other tissue-specific
1051 HIF1a peaks (combination of cell-type-specific peaks from heart, T-cells, and melanocytes).

1052 **(G)** Genome browser view showing HIF1a enrichment at *Ascl2* and *Dlx3* loci in sgVhl OPCs (in
1053 green) compared to Cas9 control OPCs (in blue), embryonic heart (in light purple), melanocytes
1054 (in beige) and T-cells (in magenta) normalized to input. H3K27ac enrichment is also shown in
1055 sgVhl OPCs (in green) compared to Cas9 control OPCs (in blue). HIF1a and H3K27ac
1056 accumulation in sgVhl OPCs are highlighted in gray (Scale bars are 2Kb).

1057 **(H)** Quantification of the percentage of early O4+, intermediate O1+, and late MBP+
1058 oligodendrocytes in both sgAscl2 (in yellow) and sgDlx3 (in dark blue) CRISPRA OPCs compared
1059 to CRISPRA sgControl (in light blue) OPCs at day 1, 2 and 3 of differentiation. Data are presented
1060 as mean ± SD of 6-8 technical replicates (individual wells) per condition.

1061 **(I)** qRT-PCR of *Sox10* in CRISPRA sgAscl2 (in yellow) and CRISPRA sgDlx3 (in dark blue)
1062 compared to CRISPRA sgControl OPCs normalized to endogenous loading control *Rpl13a*. Data
1063 are presented as mean ± SEM from 3 biological replicates (independent experiments) with 3-4
1064 technical replicates (individual wells) per experiment. p-values were calculated using Student's
1065 two-tailed t-test.

1066 See also Figure S3.

FIGURE S3

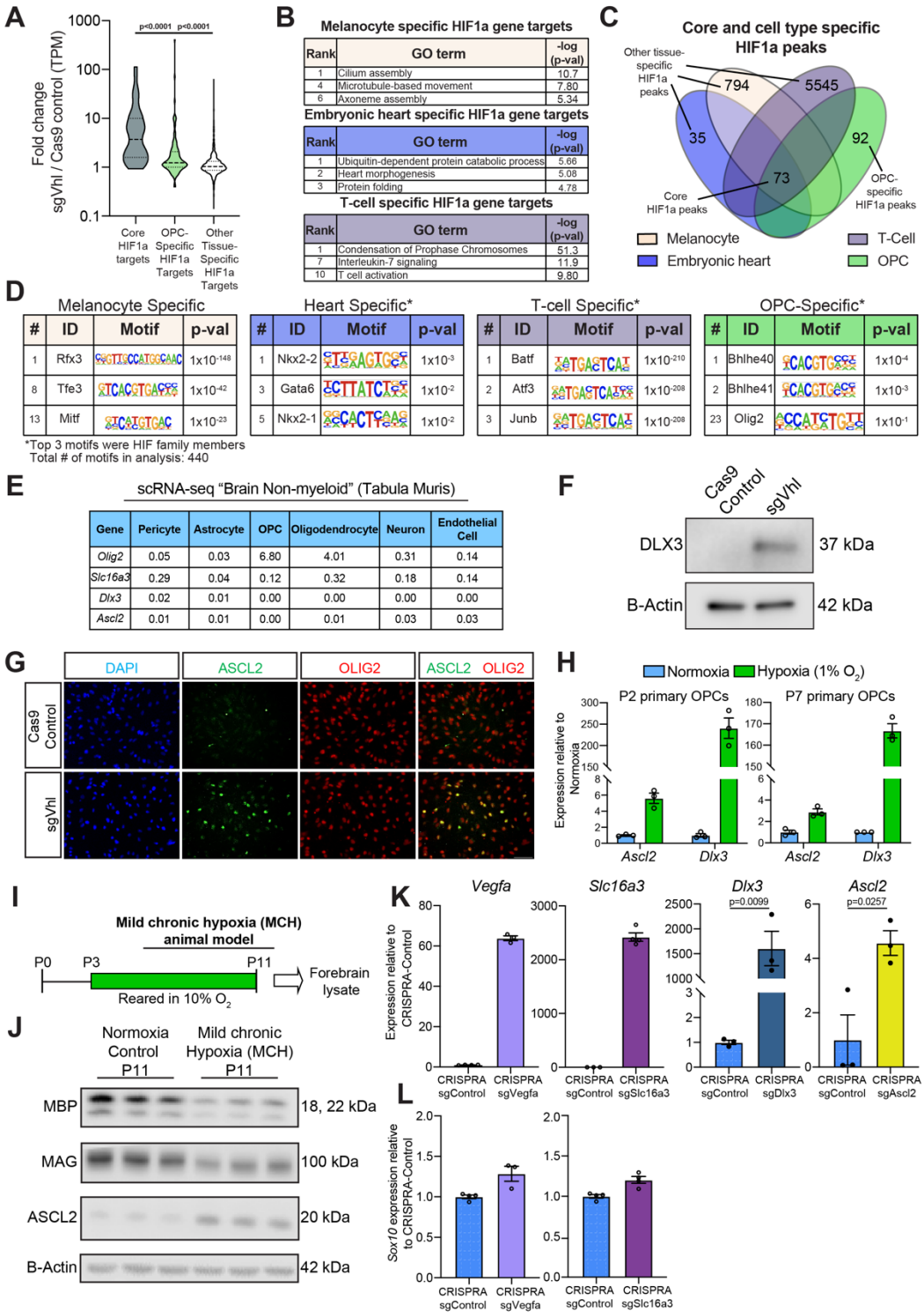

Figure S3. OPC-specific HIF1a Targets Downregulate Sox10, Related to Figure 3.

(A) Violin plot of fold change in expression (TPM) between Cas9 control and sgVhl OPCs of genes included in core (in dark gray), OPC-specific (light green) and other tissue-specific (light gray)

1072 HIF1a target categories. Bold dashed line represents the median with the thin dashed lines
1073 representing the upper and lower quartiles. p-values were calculated using the Kruskal Wallis
1074 One-Way ANOVA with Dunn's multiple comparisons test.

1075 **(B)** Gene ontology (GO) analysis of genes targeted by HIF1a specifically in melanocytes (beige),
1076 embryonic heart (purple), and T-cells (magenta). The chart includes curated pathways with their
1077 rank based on their respective p-values.

1078 **(C)** Overlap of significant HIF1a peaks (FDR<0.001) across 4 different cell types giving core
1079 HIF1a peaks, OPC-specific HIF1a peaks and other tissue-specific HIF1a peaks (combination of
1080 heart, T-cell and melanocyte specific peaks).

1081 **(D)** Table of known motifs significantly enriched in cell-type-specific HIF1a peaks in melanocytes
1082 (beige), heart (purple), T-cells (magenta) and OPCs (light green). Charts display the transcription
1083 factor name, motif, and p-value ranked in order of significance (# indicates rank out of all 440
1084 motifs in the analysis and * indicates that HIF motifs were removed).

1085 **(E)** Chart of publicly available single-cell RNA-seq data from non-myeloid cells of the brain for
1086 expression of *Dlx3*, *Ascl2* and *Slc16a3* with positive control *Olig2*, which marks OPCs and
1087 oligodendrocytes. Values are ln(1+CPM). CPM is counts per million reads.

1088 **(F)** Western blot of nuclear lysates for DLX3 in sgVhl OPCs and CRISPR-control OPCs with B-
1089 Actin as the loading control. Molecular weight is indicated to the right of the blot.

1090 **(G)** Immunocytochemistry (ICC) for ASCL2 (in green) and OLIG2 (in red) in Cas9 control and
1091 sgVhl OPCs. Nuclei are marked by DAPI (in blue).

1092 **(H)** qRT-PCR of *Dlx3* and *Ascl2* in P2 and P7 primary *in vivo* derived OPCs treated with
1093 physiological hypoxia (1% O_2, in green) compared to normoxia (21% O_2, in blue) normalized to
1094 endogenous loading control *Rpl13a*. Data are presented as mean ± SEM from 3 technical
1095 replicates (individual wells) per condition.

1096 **(I)** Schematic highlighting the mild chronic hypoxia model of diffuse white matter injury in which
1097 mouse pups are reared in 10% oxygen from postnatal day 3 to 11 (P3 to P11) to model diffuse
1098 white matter injury of prematurity. Animals are sacrificed at postnatal day (P11) and their
1099 forebrains are isolated and lysed for protein.

1100 **(J)** Western blots of forebrain lysates from P11 female C57Bl6 mice of myelin proteins MBP and
1101 MAG along with ASCL2 in animals reared in hypoxia from P3-P11 compared to control normoxic
1102 reared mice. B-Actin is shown as a loading control. N= 3 female C57Bl6 mice per treatment group.
1103 Molecular weight is indicated to the right of the blot.

1104 **(K)** qRT-PCR of *Vegfa*, *Slc16a3*, *Ascl2* and *Dlx3* normalized to endogenous loading control
1105 *Rpl13a* in their respective CRISPRA OPCs compared to CRISPRA sgControl OPCs. Data are
1106 presented as mean ± SEM from 3-4 technical replicates (individual wells) per condition.

1107 **(L)** qRT-PCR of *Sox10* in CRISPRA sgVegfa (light purple) and CRISPRA sgSlc16a3 (in
1108 magenta), OPCs compared to CRISPRA sgControl OPCs normalized to endogenous loading
1109 control *Rpl13a*. Data for CRISPRA sgVegfa and CRISPRA sgSlc16a3 are presented as mean ±
1110 SEM from 3-4 technical replicates (individual wells) per condition.

1111 **FIGURE 4**

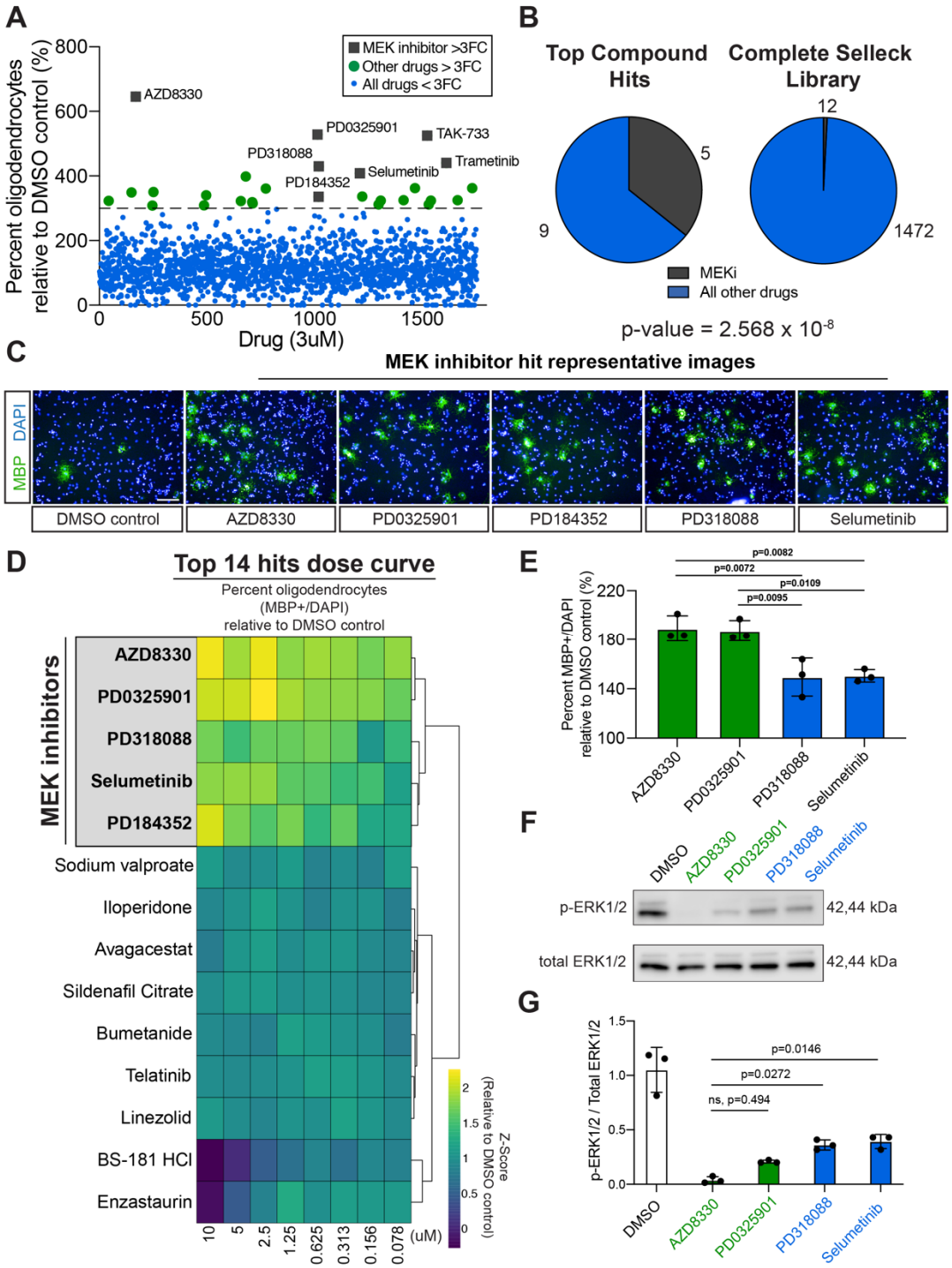

1112

1113 **Figure 4. Chemical Inhibition of MEK/ERK Increases Oligodendrocyte Formation from**
1114 **sgVhl OPCs**

1115 **(A)** Primary bioactives library screen showing the effect of 1753 molecules on percentage of
1116 oligodendrocytes (MBP+ cells/ total DAPI) formed by sgVhl OPCs relative to DMSO treated sgVhl

1117 OPCs. Anything above the dotted line represents a greater than 3-fold change increase in
1118 percentage of oligodendrocytes from DMSO (green dots). MEK inhibitors are highlighted as gray
1119 boxes with their respective drug names.

1120 **(B)** Pie charts of the number of non-toxic MEK inhibitors (in dark gray) compared to other classes
1121 of drugs (in blue) within top compound hits compared to their prevalence in the non-toxic
1122 compounds of the Selleck library. p-value was calculated using hypergeometric analysis.

1123 **(C)** Representative ICC images of oligodendrocytes (MBP+ in green) from the primary drug
1124 screen of the 5 top MEK inhibitor hits along with the DMSO negative control. Nuclei are marked
1125 by DAPI (in blue). Scale bars, 100μm.

1126 **(D)** Heatmap representation of the top 14 hits in an 8-point dose curve in 2-fold dilutions from
1127 10μM to 78nM showing the fold change in the percentage (MBP+/total DAPI) of oligodendrocytes
1128 relative to DMSO treated sgVhl OPCs. The heatmap is shown as row Z-score, and rows are
1129 sorted by unsupervised hierarchical clustering with columns in order from high (10μM) to low dose
1130 (78nM). MEK inhibitors are highlighted in gray and bolded. Data are presented as the mean for
1131 each drug at each dose from 3 separate dose curve plates.

1132 **(E)** Collapsing all tested doses into one overall average shows the ability of each MEK inhibitor
1133 to increase the formation of oligodendrocytes (MBP+/DAPI) relative to DMSO treated sgVhl
1134 OPCs. AZD8330 and PD0325901 are shown in green representing the most effective drugs, while
1135 PD318088 and Selumetinib are shown in blue as slightly less effective drugs. Data are presented
1136 as the mean ± SD of the averages of all 8 doses for each drug from 3 separate dose curve plates.
1137 p-values were calculated using a one-way ANOVA with Tukey's multiple comparisons test.

1138 **(F)** Representative Western blot for phosphorylated ERK1/2 (p-ERK1/2) relative to total ERK1/2
1139 from whole cell lysates of sgVhl OPCs incubated with 100nM of AZD8330, PD0325901,
1140 PD318088 or Selumetinib for 30 minutes. Molecular weight is indicated to the right of the blot.

1141 **(G)** Quantification of the ratio of phosphorylated ERK1/2 relative to total ERK1/2 for AZD8330 and
1142 PD0325901 (both in green) and PD318088 and Selumetinib (both in blue). Data are presented
1143 as mean ± SD from 3 biological replicates (independent experiments) with a single technical
1144 replicate per experiment. p-values were calculated using one-way ANOVA with Dunnett's multiple
1145 comparisons test.

1146 See also Figure S4.

1147 **FIGURE S4**

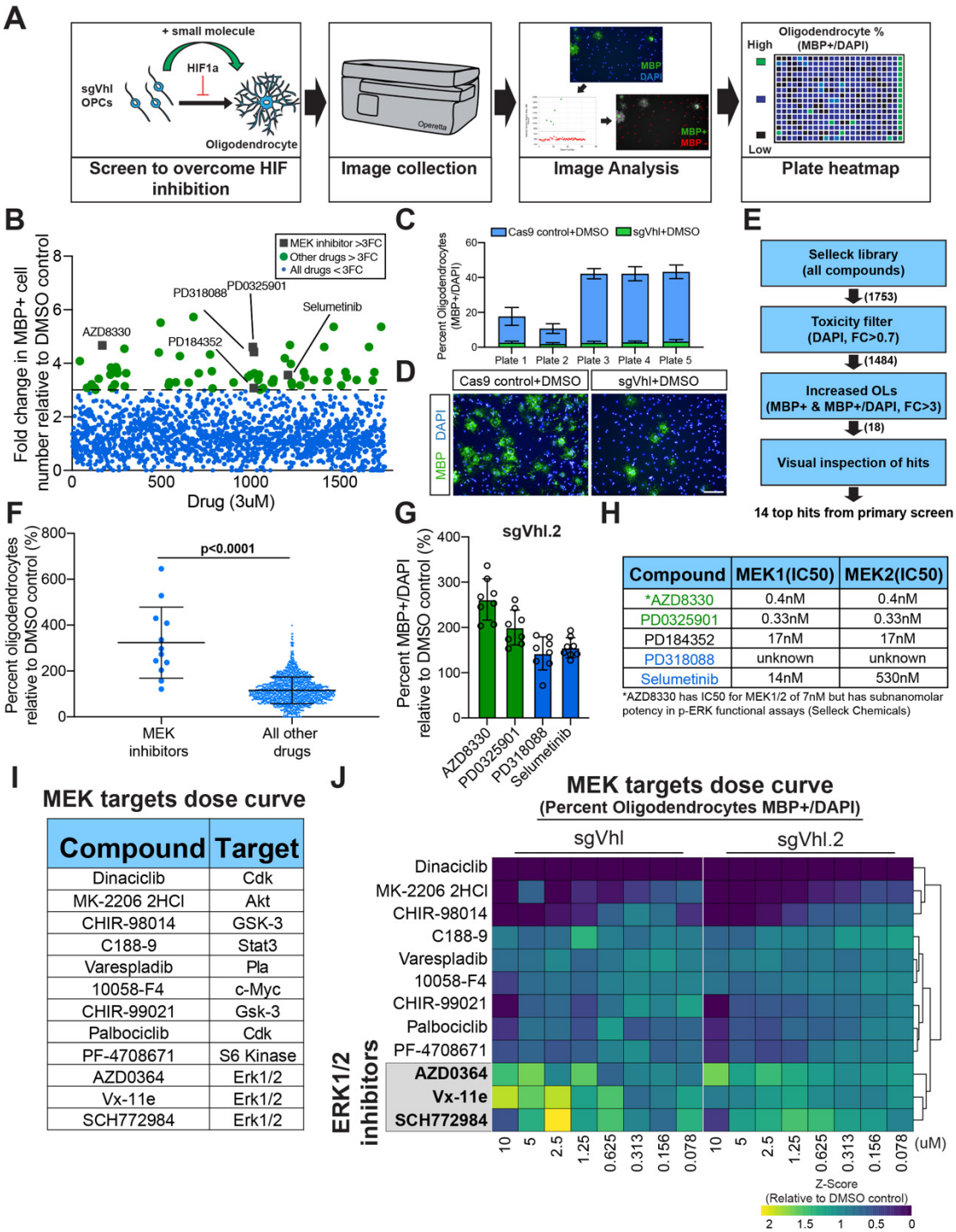

1148

1149 **Figure S4. Inhibition of MEK/ERK Signaling Increases Oligodendrocyte Formation from**
1150 **sgVhl OPCs, Related to Figure 4.**

1151 **(A)** Schematic depicting the procedure for the primary bioactives screen to uncover compounds
1152 that increase oligodendrocyte formation from sgVhl OPCs.

1153 **(B)** Primary bioactives library screen showing the effect of 1753 small molecules on number of
1154 oligodendrocytes (MBP+ cells) formed by sgVhl OPCs relative to DMSO treated sgVhl OPCs.
1155 Anything higher than the dotted line represents a greater than 3-fold change increase from DMSO
1156 (green dots). MEK inhibitors are highlighted as gray boxes with their respective drug names.

1157 **(C)** Primary screen positive control (Cas9 control+DMSO) and negative control (sgVhl+DMSO)
1158 percent oligodendrocyte (MBP+/DAPI) metrics on a per plate basis. Data represent mean ± SD
1159 from 16 technical replicates (individual wells) per plate per condition.

1160 **(D)** Representative immunocytochemistry images of oligodendrocytes (MBP+ in green) from
1161 primary screen positive (Cas9 control+DMSO) and negative (sgVhl+DMSO) controls. Nuclei are
1162 marked by DAPI (in blue). Scale bars, 100μm.

1163 **(E)** Schematic detailing the filtering steps starting with the bioactives library and narrowing down
1164 to top hits that are non-toxic (total DAPI FC<0.7), increased the number and percentage of
1165 oligodendrocytes (FC>3) and passed visual inspection to give the top 14 compound hits. Numbers
1166 in parentheses represent the number of drugs after each filtering step.

1167 **(F)** Quantification of the effect of all non-toxic MEK inhibitors (n=12) compared to all other non-
1168 toxic drugs from the primary screen (n=1472) on the percentage of oligodendrocytes from sgVhl
1169 OPCs relative to DMSO treated sgVhl OPCs. Data are presented as mean ± SD. p-values were
1170 calculated using the Mann-Whitney t-test.

1171 **(G)** Collapsing all tested doses into one overall average shows the ability of each MEK inhibitor
1172 to increase the formation of oligodendrocytes (MBP+/DAPI) from sgVhl.2 OPCs relative to DMSO
1173 treatment. AZD8330 and PD0325901 are shown in green representing the most effective drugs,
1174 while PD318088 and Selumetinib are shown in blue as slightly less effective drugs. Data are
1175 presented as the mean ± SD of all 8 doses for each drug from a single dose curve plate.

1176 **(H)** Table of IC50 values for MEK1 and MEK2 for the top MEK inhibitors AZD8330, PD035901,
1177 PD184352, and Selumetinib. IC50 is still currently unknown for PD318088.

1178 **(I)** List of the 12 drugs included on the MEK targets dose curve plate including the drug name and
1179 canonical target of the drug.

1180 **(J)** Heatmap representation of the 8-point dose curve performed for all 12 drugs in the MEK target
1181 dose curve plate shown as row Z-score. Data in the heatmap is the fold change in percent
1182 oligodendrocytes (MBP+/total DAPI) in sgVhl and sgVhl.2 OPCs relative to their respective DMSO
1183 negative controls. Rows were sorted by unsupervised hierarchical clustering and columns are in
1184 order from high (10μM) to low dose (78nM) of drug. ERK1/2 inhibitors are highlighted in gray and
1185 bold. Data are presented as the mean for each drug at each dose from 2 separate dose curve
1186 plates for both sgVhl and sgVhl.2 OPCs.

1187 **FIGURE 5**

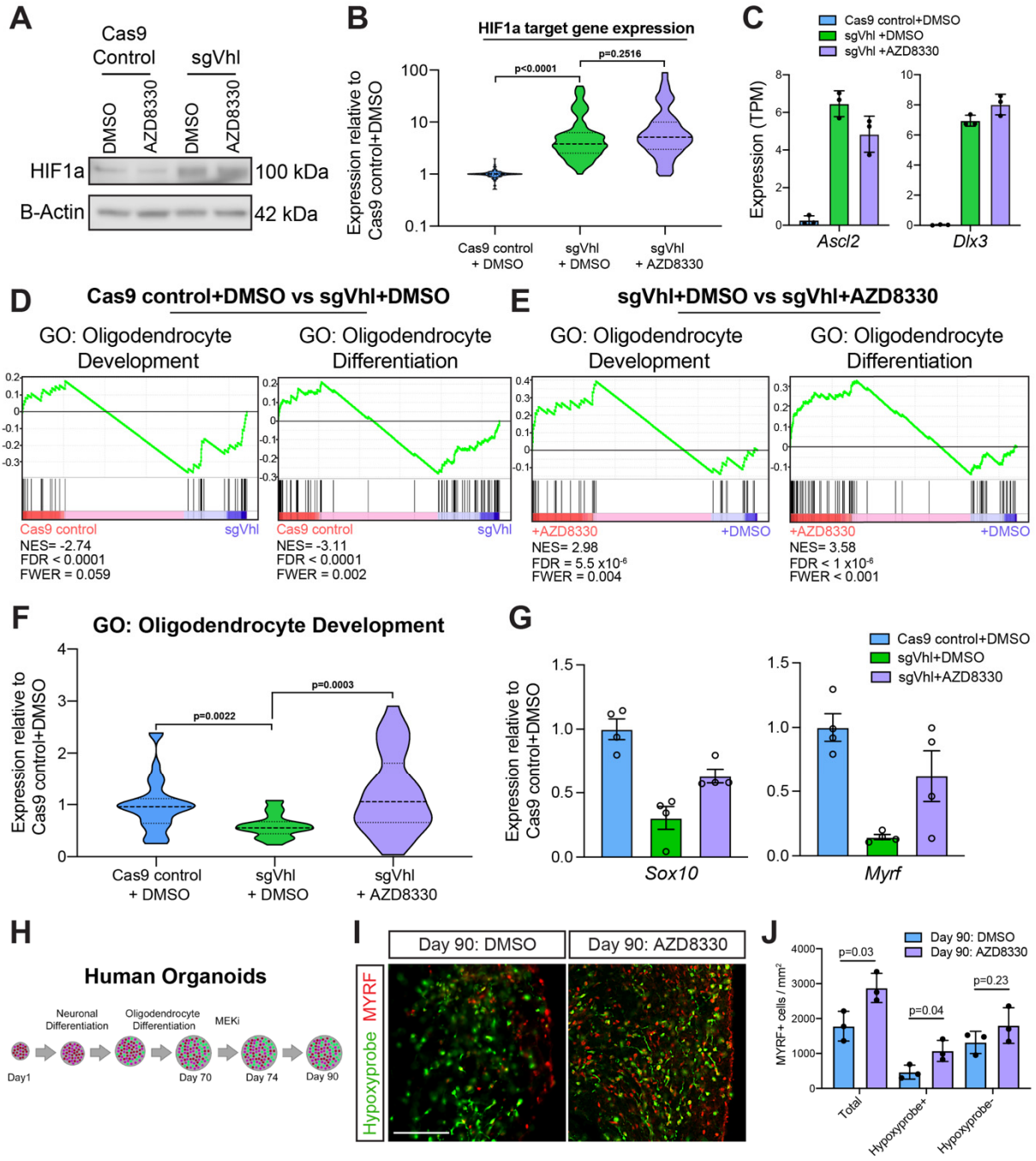

1188

1189 **Figure 5. MEK Inhibitors Restore *Sox10* Expression without Changing HIF1a activity in**
1190 **OPCs**

1191 **(A)** Western blot of nuclear lysates for HIF1a in sgVhl OPCs with 24hrs of 300nM AZD8330
1192 treatment compared to DMSO with B-Actin as a loading control. Molecular weight is indicated to
1193 the right of the blot.

(B) Violin plot of normalized number of transcripts (TPM values normalized to Cas9 control+DMSO) in Cas9 control+DMSO (in blue), sgVhl + DMSO (in green), and sgVhl + AZD8330 (in purple) relative to Cas9 control + DMSO of genes that were previously shown to be direct targets of HIF and increase in sgVhl OPCs compared to control (see Figure 2B). p-values were calculated using the Kruskal Wallis One-Way ANOVA with Dunn's multiple comparisons test.

(C) Quantification of the normalized number of transcripts (TPM) for both *Ascl2* and *Dlx3* in Cas9 control+DMSO (in blue), sgVhl+DMSO OPCs (in green) and sgVhl+AZD8330 OPCs (in purple). OPCs were treated with either DMSO or 300nM AZD8330 for 14 hours. Data represent mean ± SD from 3 biological replicates (independent samples) from RNA-seq.

(D) Gene set enrichment analysis (GSEA) analysis of gene program changes in sgVhl compared to Cas9 control OPCs demonstrates a significant reduction in GO terms for Oligodendrocyte Development (normalized enrichment score/NES = -2.74, FDR<0.0001, FWER p-val = 0.059) and Oligodendrocyte Differentiation (NES = -3.11, FDR<0.0001, FWER p-val = 0.002).

(E) GSEA analysis of gene program changes in sgVhl + AZD8330 compared to sgVhl + DMSO OPCs demonstrates a significant enrichment in GO terms for Oligodendrocyte Development (normalized enrichment score/NES = 2.98, FDR= 5.5×10^{-6}, FWER p-val = 0.004) and Oligodendrocyte Differentiation (NES = 3.58, FDR<1×10^{-6}, FWER p-val <0.001).

(F) Violin plot showing expression of transcripts (TPM values normalized to Cas9 control + DMSO OPCs) associated with GO term Oligodendrocyte Development (GO:0014003) that decrease (FC<0.75) in sgVhl + DMSO OPCs (in green) relative to Cas9 control + DMSO OPCs (in blue) as well as sgVhl OPCs following treatment with 300nM AZD8330. p-values were calculated using the Kruskal Wallis One-Way ANOVA with Dunn's multiple comparisons test.

(G) qRT-PCR of *Sox10* and *Myrf* in Cas9 control+DMSO (in blue), sgVhl+DMSO (in green) and sgVhl+AZD8330 OPCs (in purple) normalized to endogenous control *Rpl13a*. OPCs were treated with either DMSO or 300nM AZD8330 for 14 hours. Data are presented as mean ± SEM from 4 technical replicates (individual wells).

(H) Schematic of human brain oligocortical spheroids treated at days *in vitro* 70 with either DMSO or 300nM AZD8330 for 4 days. The spheroids were then cultured without drug until day 90 when they were incubated with hypoxyprobe, fixed and then sectioned for immunohistochemistry.

(I) Representative immunohistochemistry images of DIV 90 oligocortical spheroids that had been treated from DIV 70-74 with either DMSO or 300nM AZD8330 for oligodendrocytes (MYRF+ in red) and hypoxic regions (hypoxyprobe in green). Scale bar, 100μM.

(J) Quantification of oligodendrocytes (MYRF+ / mm^2) in the whole oligocortical spheroid (total), hypoxic region of the spheroid (hypoxyprobe+), and normoxic region of the spheroid (hypoxyprobe-) in DIV 90 spheroids that had been treated with either DMSO or 300nM AZD8330 from DIV 70-74. Data represent mean ± SD from 3 biological replicates (individual spheroids). p-values were calculated using Student's two-tailed t-test.

See also Figure S5.

1232 **FIGURE S5**

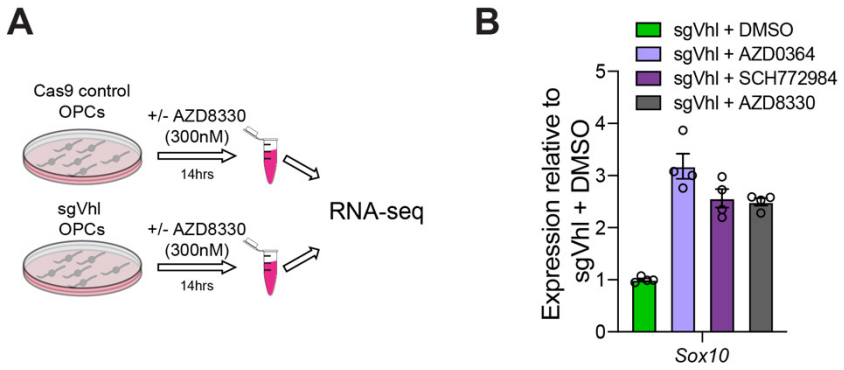

1233

1234 **Figure S5. Inhibition of MEK/ERK Signaling Drives *Sox10* Expression in sgVhl OPCs,**
1235 **Related to Figure 5**.

1236 **(A)** Schematic highlighting the setup of the RNA-seq experiment in which Cas9 control and sgVhl
1237 OPCs were treated with either DMSO or 300nM of AZD8330 for 14 hours and then cells were
1238 lysed for poly-adenylated mRNA extraction and sequenced.

1239 **(B)** qRT-PCR of *Sox10* in sgVhl OPCs treated with DMSO, AZD0364 (1μM, in purple),
1240 SCH772984 (1μM, in magenta) or AZD8330 (300nM, in gray) for 14hrs normalized to endogenous
1241 control *Rpl13a*. Data are presented as mean ± SEM from 4 technical replicates (individual wells)
1242 per condition.